Received: 26 September 2018 | Revised: 13 November 2018 | Accepted: 20 November 2018

DOI: 10.1002/wcms.1411

WIREs COMPUTATIONAL MOLECULAR SCIENCE WILEY

ADVANCED REVIEW

Ab initio nonadiabatic molecular dynamics investigations on the excited carriers in condensed matter systems

Qijing Zheng[1] | Weibin Chu[1] | Chuanyu Zhao[1] | Lili Zhang[1] | Hongli Guo[1,2] | Yanan Wang[1] | Xiang Jiang[1] | Jin Zhao[1,3,4]

[1]ICQD/Hefei National Laboratory for Physical Sciences at Microscale, and Key Laboratory of Strongly-Coupled Quantum Matter Physics, Chinese Academy of Sciences, and Department of Physics, University of Science and Technology of China, Hefei, China

[2]School of Physics and Technology, Center for Nanoscience and Nanotechnology, and Key Laboratory of Artificial Micro- and Nano-structures of Ministry of Education, Wuhan University, Wuhan, China

[3]Department of Physics and Astronomy, University of Pittsburgh, Pittsburgh, Pennsylvania

[4]Synergetic Innovation Center of Quantum Information & Quantum Physics, University of Science and Technology of China, Hefei, China

Correspondence
Jin Zhao, ICQD/Hefei National Laboratory for Physical Sciences at Microscale, and Key Laboratory of Strongly-Coupled Quantum Matter Physics, Chinese Academy of Sciences, and Department of Physics, University of Science and Technology of China, Hefei, Anhui 230026, China.
Email: zhaojin@ustc.edu.cn

Funding information
Fundamental Research Funds for the Central Universities of China, Grant/Award Number: WK3510000005; National Natural Science Foundation of China, Grant/Award Numbers: 11704363, 11620101003, 21421063; National Key Foundation of China, Grant/Award Numbers: 2016YFA0200604, 2017YFA0204904

The ultrafast dynamics of photoexcited charge carriers in condensed matter systems play an important role in optoelectronics and solar energy conversion. Yet it is challenging to understand such multidimensional dynamics at the atomic scale. Combining the real-time time-dependent density functional theory with fewest-switches surface hopping scheme, we develop time-dependent ab initio nonadiabatic molecular dynamics (NAMD) code Hefei-NAMD to simulate the excited carrier dynamics in condensed matter systems. Using this method, we have investigated the interfacial charge transfer dynamics, the electron–hole recombination dynamics, and the excited spin-polarized hole dynamics in different condensed matter systems. The time-dependent dynamics of excited carriers are studied in energy, real and momentum spaces. In addition, the coupling of the excited carriers with phonons, defects and molecular adsorptions are investigated. The state-of-art NAMD studies provide unique insights to understand the ultrafast dynamics of the excited carriers in different condensed matter systems at the atomic scale.

This article is categorized under:
Structure and Mechanism > Computational Materials Science
Molecular and Statistical Mechanics > Molecular Dynamics and Monte-Carlo Methods
Electronic Structure Theory > Ab Initio Electronic Structure Methods
Software > Simulation Methods

KEYWORDS
excited carrier dynamics, Hefei-NAMD, nonadiabatic molecular dynamics, real-time time-dependent density functional theory

1 | INTRODUCTION

Excited carrier dynamics play an important role in different research areas. For example, significant efforts have been devoted to search for environmentally friendly materials for solar energy conversion,[1–6] in which the efficiency strongly depends on the dynamics of the photogenerated electron–hole (e–h) pairs. In photovoltaics and photocatalysis, it is important to separate the e–h pairs, increasing the lifetime of the excited carriers so that the photoenergy can be changed to electric or chemical energy through these excited carriers. The charge transfer dynamics of excited charge carrier to the adsorbed molecules are important for the photocatalysis reactions. Therefore, to improve the solar energy conversion efficiency, it is important to understand the crucial factors which determine the pathway and timescale of charge transfer and e–h recombination. In

addition, for photonic device applications, several important figures of merit are closely linked to photogenerated carrier dynamics.[7–12] For instance, for the application in light emitting devices, it is crucial to suppress the nonradiative e–h recombination. In the contrary, for the applications as optical switches, the lifetime of excited carrier is required to be short so that there can be a fast response. Thus, it is highly desirable to control the photocarrier behavior in different materials, including relaxation pathways and dynamics, to suit the needs of various device functionalities. Moreover, for the newly developed quantum materials,[3,13] the elementary excitation properties are essential to be investigated and understood.

In recent decades, ab initio theoretical calculations based on density functional theory (DFT) have been widely used to investigate the electronic structure of condensed matter systems and great success has been achieved. Beyond DFT level, GW approximation based on many-body theory has been used to correct the quasi-particle energy levels obtained by DFT.[14–18] Together with the Bethe–Salpeter equation (BSE), the binding energy of exciton can be obtained and the optical spectra can be simulated.[19–25] In addition to that, linear response time-dependent DFT (LR-TDDFT) has also been used to study the excitation energies.[26,27] Great achievements have been obtained for the investigation of the ground and excited states in condensed matter systems based on these methods, yet usually only the static electronic structure information can be obtained based on these methods. The dynamics of the excited carriers, however, cannot be investigated based on these methods.

To investigate the excited carriers dynamics, other methods, such as molecular dynamics (MD), which directly mimics the real-time dynamical process, is necessary. Conventional MD is based on two assumptions: (a) the Born–Oppenheimer (adiabatic) approximation which separates the electronic and nuclei motion, reducing the nuclei motion on a single adiabatic potential energy surface (PES) and (b) the classical treatment of the nuclei. Processes such as electron transfer,[28–30] charge transport, electronic friction at metal surfaces[31,32] and nonradiative decay after photoexcitation often involve multiple PESs, with nonadiabatic (NA) transitions among them. In addition, for systems containing small mass elements, for example, hydrogen, zero-point motion and tunneling effects may not be ignored and as a result require a quantum mechanical description of the nuclei.[33–35] To address all these issues, the most ambitious approach is to treat the entire system, including the nuclei, quantum-mechanically. Unfortunately, the formidable computational costs restrict the scope of the application and can only be applied to small systems within short time scales under the current computation resources. If the nuclear quantum effects are known to be unimportant, then one can proceed via a mixed quantum-classical (MQC) method, where only the electrons are treated quantum mechanically while the nuclei are considered as classical particles.

The key issue in the MQC method is the quantum-classical self-consistency (QCSCF) problem: the quantum subsystem must propagate correctly under the influence of the classical subsystem, with transitions between the quantum states along the evolution; meanwhile, the classical subsystem must respond accordingly to the quantum transitions, which comprises the so-called "quantum-backreaction" problem.[36] A proper treatment of the latter is especially challenging. In this regard, the two most widely used methods are Ehrenfest method (also known as mean-field method) and surface hopping method. In the mean-field approach, the classical subsystem evolves on a single PES, which is weight-averaged over the quantum states. The method is invariant to the choice of quantum representation, conserves the total energy and usually provides good description of the transition probabilities. However, the correlation between the quantum and classical subsystems is not correctly described, which means that this approach is valid when the different quantum states involved in the dynamics are not significantly different.[37–39] Surface hopping method was proposed to deal with the quantum-classical correlation by introducing stochastic hops between different PESs.[40,41] The hopping algorithm is not unique and the most popular one is Tully's fewest-switches algorithm.[41] In addition, surface hopping satisfies microscopic reversibility while Ehrenfest method does not.[36] For a comprehensive review of the two methods, please refer to References 36–40,42. As to the quantum evolution part of the QCSCF, one can proceed via real-time time-dependent DFT (RT-TDDFT) where the quantum-backreaction is treated in the Ehrenfest scheme, as is implemented in octopus[43] and Time Dependent Ab-initio Package (TDAP).[44,45] A more general way is to expand the electronic wavefunction in a basis set (representation), the Schrödinger equation then becomes a set of equations for the expanding coefficients. Under this scheme, the knowledge of the ground state, excited states and nonadiabatic couplings (NACs) between them are required. General quantum chemistry method can be used to generate all the information needed and it has been implemented in a few codes.[40,46–51] In addition, Tavernelli and coworkers[52] showed that the necessary quantities can also be rigorously derived from LR-TDDFT. Prezhdo and coworkers[47,48,53] develop a scheme where adiabatic Kohn–Sham (KS) orbitals are used to expand the electronic wavefunction. It has been shown that the adiabatic KS orbitals can be seen as zeroth-order approximation to LR-TDDFT adiabatic states.[54] This expansion along with the so-called classical path approximation (CPA),[39,47,55] in which the nuclear dynamics of the system remains unaffected by the dynamics of the electronic degrees of freedom, significantly reduces the computational cost and can be applied to condensed matter systems with large number of atoms.

We have developed home-made time-dependent ab initio NAMD code (Hefei-NAMD) combining the TDDFT and surface hopping schemes based on CPA approximation.[56] The adiabatic KS orbitals are used as basis sets to expand the electronic wavefunction. Using this method, we have investigated the nonradiative excited carrier dynamics in different condensed matter systems including the interfacial charge transfer dynamics, the e–h recombination dynamics and the excited spin-polarized

hole dynamics. In this study, we have reviewed our recent research works related to this topic. The article is organized as follows. Section 1 introduces the method of NAMD simulation. Section 2 reviews the interfacial charge transfer dynamics at interfaces of molecule/solid and van der Waals (vdW) heterostructure formed by two-dimensional (2D) materials. Section 3 reviews the e–h recombination dynamics in doped semiconductor. Section 4 reviews the photogenerated spin hole dynamics in doped 2D MoS_2.

2 | METHODOLOGY

The ab initio NAMD simulations are carried out using home-made Hefei-NAMD code[56] which augments the Vienna ab initio simulation package (VASP) [57–59] with the NAMD capabilities within time-domain density functional theory (TDDFT) similar to References 47,48. The time-dependent KS (TDKS) orbitals $\psi_e(\mathbf{r}, t)$ are expanded in the basis of instantaneous adiabatic KS orbitals $\phi_j(\mathbf{r}, \mathbf{R}(t))$, which are obtained by solving time-independent KS equation at configuration $\mathbf{R}(t)$

$$\psi_e(\mathbf{r}, t) = \sum_j c_j(t)\phi_j(\mathbf{r}, \mathbf{R}(t)) \tag{1}$$

by inserting Equation (1) into TDKS equation,[60] a set of differential equations for the coefficients is produced:

$$i\hbar \frac{\partial}{\partial t} c_j(t) = \sum_k c_k(t)\left[\varepsilon_k \delta_{jk} - i\hbar \mathbf{d}_{jk}(t)\right] \tag{2}$$

The square modulus of the coefficients, $|c_j(t)|^2$, can be explained as the population of the corresponding KS orbitals. Here, ε_k is the energy of the adiabatic KS state and $\mathbf{d}_{jk}$ is the NACs between KS states j and k. The NAC can be written as:

$$\mathbf{d}_{jk} = \left\langle \phi_j | \frac{\partial}{\partial t} | \phi_k \right\rangle = \sum_I \frac{\left\langle \phi_j | \nabla_{\mathbf{R}_I} \mathcal{H} | \phi_k \right\rangle}{\varepsilon_k - \varepsilon_j} \cdot \dot{\mathbf{R}}_I \tag{3}$$

where $\mathcal{H}$ is the KS Hamiltonian, ϕ_j, ϕ_k, ε_j and ε_k are the wave functions and eigenvalues for electronic states j and k, and $\dot{\mathbf{R}}_I$ is velocity of the nuclei. Thus, the NACs mainly depend on the energy difference term $\varepsilon_k - \varepsilon_j$, the electron–phonon (e–p) coupling term $\left\langle \phi_j | \nabla_{\mathbf{R}_I} \mathcal{H} | \phi_k \right\rangle$ and the nuclear velocity term $\dot{\mathbf{R}}_I$.

The NACs are calculated in a finite difference method.[61,62] With the coefficients $c_j(t)$ and the NACs, hopping probabilities between the adiabatic KS states according to Tully's fewest-switches algorithm can be obtained as[41]:

$$P_{j\to k}(t, \Delta t) = \frac{2\Re\left[c_j^* c_k \mathbf{d}_{jk}\right]\Delta t}{c_j^* c_j} \tag{4}$$

Further, the probabilities are multiplied by a Boltzmann factor within the CPA.[47] Besides FSSH, the decoherence-induced surface hopping was also implemented in Hefei-NAMD.[63]

The time-dependent real-space information of the photocarrier can be obtained as the norm-square of the time-dependent KS orbitals $|\psi_e(\mathbf{r}, t)|^2$. By expanding using Equation (1), we have

$$\rho(\mathbf{r}, t) = |\psi_e(\mathbf{r}, t)|^2 = \sum_j c_j^*(t)c_j(t)\phi_j^*(\mathbf{r}, \mathbf{R}(t))\phi_j(\mathbf{r}, \mathbf{R}(t)) \tag{5}$$

A further separation of the above quantity can be obtained by taking the time derivative of Equation (5):

$$\begin{aligned} \frac{d\rho(\mathbf{r}, t)}{dt} &= \sum_j \left[\frac{d}{dt} c_j^*(t)c_j(t)\right]\phi_j^*(\mathbf{r}, \mathbf{R}(t))\phi_j(\mathbf{r}, \mathbf{R}(t)) \\ &\quad + c_j^*(t)c_j(t)\left[\frac{d}{dt}\phi_j^*(\mathbf{r}, \mathbf{R}(t))\phi_j(\mathbf{r}, \mathbf{R}(t))\right] \end{aligned} \tag{6}$$

As can be seen from Equation (6), the time variation can be clearly divided into two parts: a change primarily due to the variation of the KS states populations $c_j^*(t)c_j(t)$, which comes from the first part of the equation and we denotes it as the NA contribution. This corresponds to the process indicated by the blue arrow in Figure 1. For the second part of the equation, the time variation derives from the change of the adiabatic KS orbitals and as a result, we refer to this part as the adiabatic contribution (AD) as is shown by the red arrow in Figure 1.[64]

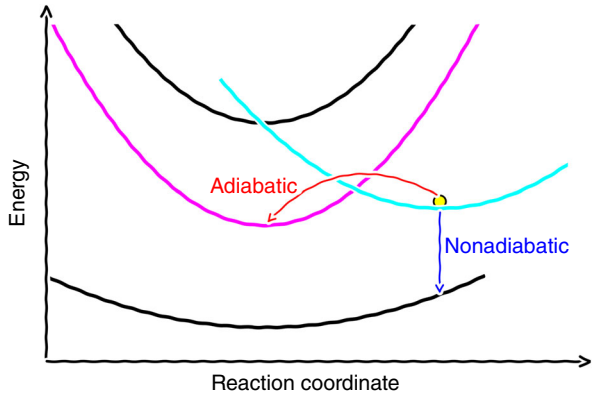

FIGURE 1 Schematics of the adiabatic (red solid line) and nonadiabatic (blue solid line) charge transfer process. The solid black lines represent the potential energy surface

For condensed matter system, the knowledge of the dynamics in the momentum space is also very important. To include the phonon contribution from different momentum, usually the ab initio MD is performed using a supercell with Brillouin Zone (BZ) sampled only at Γ point. In this case, the k-points of the primitive cell BZ are folded onto the Γ point of the supercell BZ. The band structure unfolding can be realized as discussed in Reference 65. Zheng also developed a home-made band unfolding code for VASP calculations.[66]

3 | INTERFICIAL CHARGE TRANSFER DYNAMICS

3.1 | Ultrafast dynamics of photogenerated holes at a CH_3OH/TiO_2 rutile interface

TiO_2 is a wide band gap semiconductor which has important applications in photocatalysis and photovoltaics. The ultrafast charge transfer dynamics of the photogenerated carriers at the aqueous/TiO_2 surface are important for the solar energy conversion efficiency.[67–81] CH_3OH is known as hole scavenger which can trap the photogenerated holes at TiO_2 surface and Chu et al.[82] investigated the photogenerated hole dynamics at CH_3OH/TiO_2 using ab initio NAMD simulations. The forward and reverse hole transfer processes as well as the hot hole relaxation between TiO_2 and CH_3OH were studied. The hole-scavenging ability of CH_3OH with different adsorption structures were investigated too.

3.1.1 | Forward hole transfer from TiO_2 to adsorbates

The forward hole transfer was defined to be the hole transfer from TiO_2 to adsorbates. In such a process the TiO_2 bulk states and highest occupied molecular orbitals (HOMOs) of CH_3OH act as the donor and acceptor states, respectively. The efficiency of such a process determines the hole-scavenging ability of the adsorbates. To investigate such a process, photogenerated holes at −0.4, −0.6, −1.0 eV below the averaged HOMO energy over the two CH_3OH molecules and over MD trajectory at 100 K (E_{HOMO}) were generated as initial holes. The forward hole transfer properties at CH_3OH/TiO_2 of different adsorption structures (molecular, half-dissociated and fully dissociated, labeled as M, HD and D) are shown in Figure 2a. At $t = 0$ fs, the hole localization on TiO_2 is higher than 90% for all three structures. For the M structure, there is almost no forward hole transfer from TiO_2 to the molecule within 500 fs. For D structure, the hole transfer reaches 20% at around 300 fs and then some charge oscillation follows indicating that both forward and reverse charge transfers happen. The total hole localization on TiO_2 is kept at around 85%. This forward hole transfer is insensitive to the initial energies of the holes.

As has been discussed in the methodology part, the charge transfer process is contributed by AD and NA mechanisms. The NA mechanism corresponds to the direct tunneling or hopping between the donor and acceptor states. The AD charge transfer is provoked by the nuclear motion and often happens at the crossings of electronic states where the NAC increases distinctly because of the hybridization of different states. Fischer et al.[83] showed that both of these two mechanisms contribute to the charge transfer process. Both the NA and AD components are very small for the M structure because the hole remains largely on TiO_2. For the HD and D structures, the NA and AD mechanisms compete with each other in the forward hole transfer process. The NA mechanism contributes to the hole hopping to the molecular HOMO because it is energetically favored. The AD mechanism favors the reverse hole transfer from the molecule back to the TiO_2 surface because AD charge transfer is possible to happen whenever the HOMO of CH_3OH crosses the TiO_2 states. The NA charge transfer is dominant and this causes the partial hole transfer from TiO_2 to adsorbed molecules.

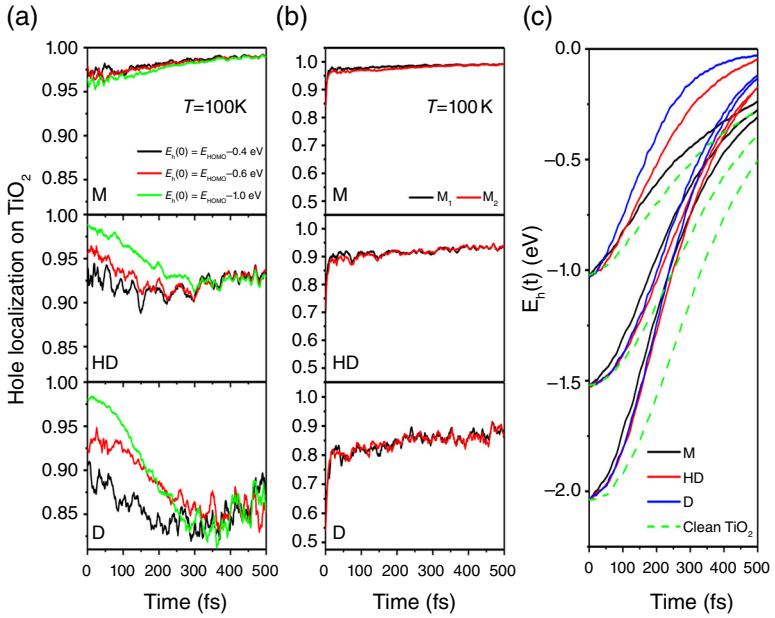

FIGURE 2 (a) Averaged forward hole transfer from TiO_2 bulk states to adsorbed molecules at 100 K. (b) Averaged reverse hole transfer from adsorbed molecules to TiO_2 bulk states at 100 K. (c) Time dependence of energy relaxation of photogenerated holes with different initial energies at 100 K. (Reprinted with permission from Reference 82. Copyright 2016 American Chemical Society)

3.1.2 | Reverse hole transfer from adsorbates to TiO_2

The reverse hole transfer process, which determines the lifetime of trapped holes, was also discussed by Chu et al.[82] The initial photogenerated hole was generated on HOMOs of CH_3OH molecules. However, because of the strong hybridization between CH_3OH and TiO_2, the initial hole state has substantial contribution from TiO_2 surface. The reverse hole transfer process was found to happen in an ultrafast way, which is within 10 fs for all different adsorption structures as shown in Figure 2b. Yet for the D structure, there is around 20% of the hole remains on CH_3OH after the initial back hole transfer process, which is possible to initiate the following photochemical reactions.

Such ultrafast reverse hole transfer process is mainly determined by the AD charge transfer mechanism. This is attributed to the high density of states (DOSs) contributed by TiO_2 at the energy of CH_3OH HOMO. Due to the e–p interaction, the HOMO state crosses TiO_2 valance band (VB) states frequently during a MD run, which lead to sufficient AD charge transfer. As discussed in Reference 82, the C—O stretching mode at 900 cm^{-1} plays an important role in the reverse hole transfer.

3.1.3 | Hole energy relaxation to VBM

Besides the forward and reverse hole transfers between molecule and TiO_2, the rate of the energy relaxation to VBM, which is induced by e–p coupling, was also discussed.[82] By taking the average energy of valence band maximum (VBM) as the reference, the time-dependent hole energy ($E_h(t)$) for a range of initial hole excitations were calculated. Figure 2c shows $E_h(t)$ at 100 K with the initial hole energies $E_h(0)$ to be −2.0, −1.5 and −1.0 eV. The three different adsorption structures and the clean TiO_2 surface were investigated. It is found that the molecular adsorption accelerates the hole relaxation to VBM. With the initial hole energy $E_h(0) = -2.0$ eV, such adsorption-induced acceleration is significant for all the M, D and HD structures. Nevertheless, for $E_h(0) = -1.0$ eV, the acceleration is only distinct for the D structure.

Such adsorption-induced acceleration can attribute to the e–p coupling of the CH_3OH HOMO, which shows strong time-dependent energy fluctuations as shown in Reference 82. Level crossings, which are induced by such fluctuations, favor the AD charge transfer and as a result additional energy relaxation channels are opened. Naturally, the molecular HOMO energies determine such acceleration. For the M structure, the HOMOs are located in the range of −2.5 to −0.8 eV and therefore the hole relaxation acceleration for $E_h(0) = -1.0$ eV is not significant. For the D structure, the HOMOs are located above −1.1 eV and thus the hole relaxation for $E_h(0) = -1.0$ eV is distinct.

Since both the hole transfer and relaxation dynamics at CH_3OH/TiO_2 interface are affected by the e–p interaction, it is interesting to investigate the temperature dependence. As shown by Chu et al.,[82] decreasing the temperature from 100 to 30 K suppress the forward hole transfer and the hole relaxation process. Recently, both the forward and reverse hole transfer were measured in CH_3OH/C_3N_4 system. It was also proved that the CH_3O is the dominate species for hole trapping.[84] The timescales for the forward and reverse hole transfer obtained in the experiments are at ps magnitude, which are much longer than the theoretical results for CH_3OH/TiO_2. This might be due to the complicated environment in the experiments which is not

included in the simulation. It should also be mentioned that the NAMD simulations by Chu et al. is based on CPA approximation, in which the nuclear dynamics are not affected by the excited holes. In this framework, the excited hole induced photochemical reactions of CH_3OH on TiO_2 cannot be studied. Kolesov et al.[85] studied the following photo-oxidation process, in which methoxy (CH_3O) converts into formaldehyde (CH_2O), using Erhenfest dynamics based on TDDFT. In their work they found that the photogenerated hole can be trapped by CH_3O in 50 fs, which is faster than what Chu et al. obtained using NAMD based on FSSH. The C—H bond cleavage happens between 50 and 75 fs. The deviation between the FSSH and the Erhenfest dynamics may be due to the different treatments and approximations in these two methods. Controlled time-resolved experiments with high accuracy are required for the benchmarks of different theoretical methods.

4 | ULTRAFAST DYNAMICS OF SOLVATED ELECTRONS AT H_2O/LAO/STO INTERFACE

Different with the photogenerated hole dynamics, the solvated electron states represent the lowest states which can be occupied by the photogenerated electrons and were proposed to be an important media in the photocatalysis at oxide/aqueous interface.[83,86–94] However, previous studies show that the solvated electron states are usually located at higher energies than the conduction band minimum (CBM), which makes them difficult to be utilized in the charge transfer processes in photocatalysis.[86,90,92,94] Therefore, the reduction of solvated electron state energies are essential to improve the efficiency of photocatalysis.

Taking $LaAlO_3/SrTiO_3$ (LAO/STO) heterostructure with one monolayer H_2O adsorption as a prototypical system, Wang et al.[95] showed that the energy and dynamics of solvated electron can be tuned by the built-in electric field in the polar–nonpolar oxide heterostructure using DFT and ab initio NAMD. Especially for LAO/STO with *p*-type interface, the solvated electron states can be stabilized distinctly by the electric field in LAO. As shown in Figure 3, the solvated electron band minimum (SEBM) decreases with the increase of the LAO thickness. When LAO is thicker than 4 unit cells (ucs), SEBM becomes CBM of the whole system. When LAO reaches 8 ucs, SEBM can even be stabilized to the Fermi level (E_f) and partially occupied.

The *p*-type LAO/STO interface can successfully stabilize the solvated electron states. However, the SEBM is still above the CBM when LAO is thinner than 4 ucs. In this case, the electrons excited to the solvated electron states will transfer back to the LAO/STO surface within a certain lifetime and such charge-transfer dynamics of solvated electrons were investigated using NAMD simulations. The time-dependent energy level evolution, electron localization in H_2O layer and averaged energy of the photogenerated solvated electron for H_2O on LAO/STO with 1–3 ucs LAO are shown in Figure 4. One can see that about 80% of the solvated electrons transfer to LAO/STO within 10 fs, showing an ultrafast behavior. Such an ultrafast

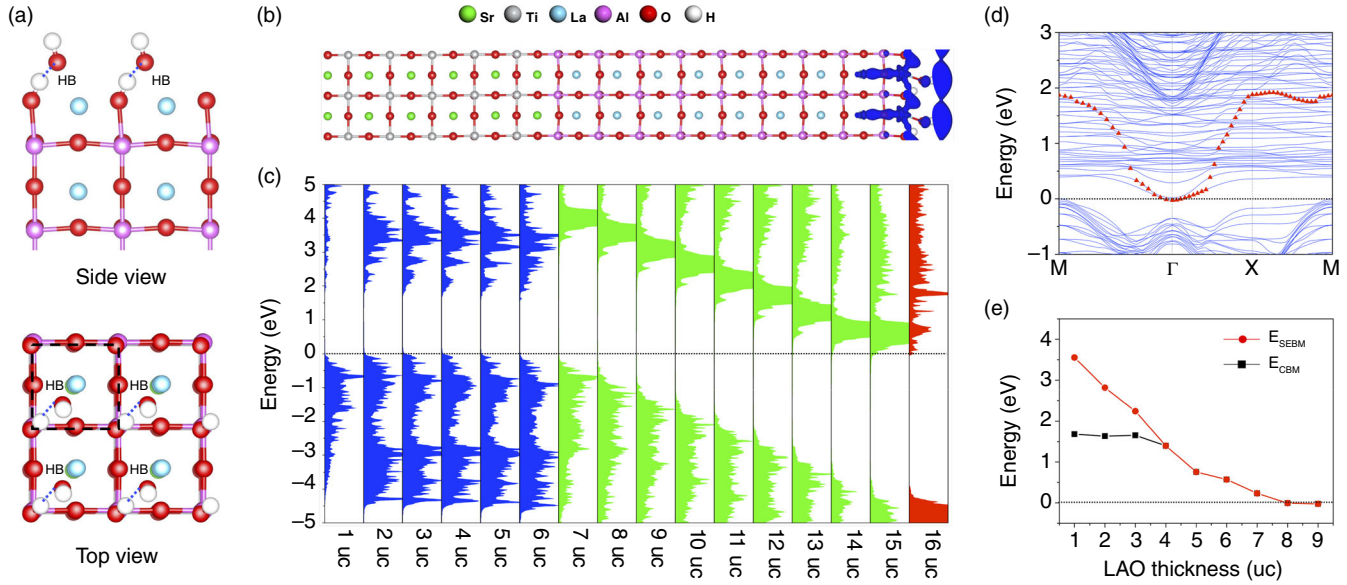

FIGURE 3 (a) Side and top views of 1ML H_2O adsorbed on *p*-type LAO/STO heterostructure. (b) Spatial orbital distribution of the solvated state in H_2O layer. (c) Layer-resolved density of state for every LAO, STO and H_2O layer, represented by green, blue and red shades. The dash line represents the position of E_f. (d) Band structure of 1ML H_2O adsorbed on *p*-type LAO/STO. The solvated electron band is marked by red triangles. (e) The dependence of solvated electron band minimum (SEBM) and conduction band minimum (CBM) energies on LAO thickness. The energy of VBM is set as the reference in (c–e). The results in (a–d) correspond to 1ML H_2O adsorbed on *p*-type LAO/STO with 9 ucs LAO. (Reprinted with permission from Reference 95. Copyright 2018 American Chemical Society)

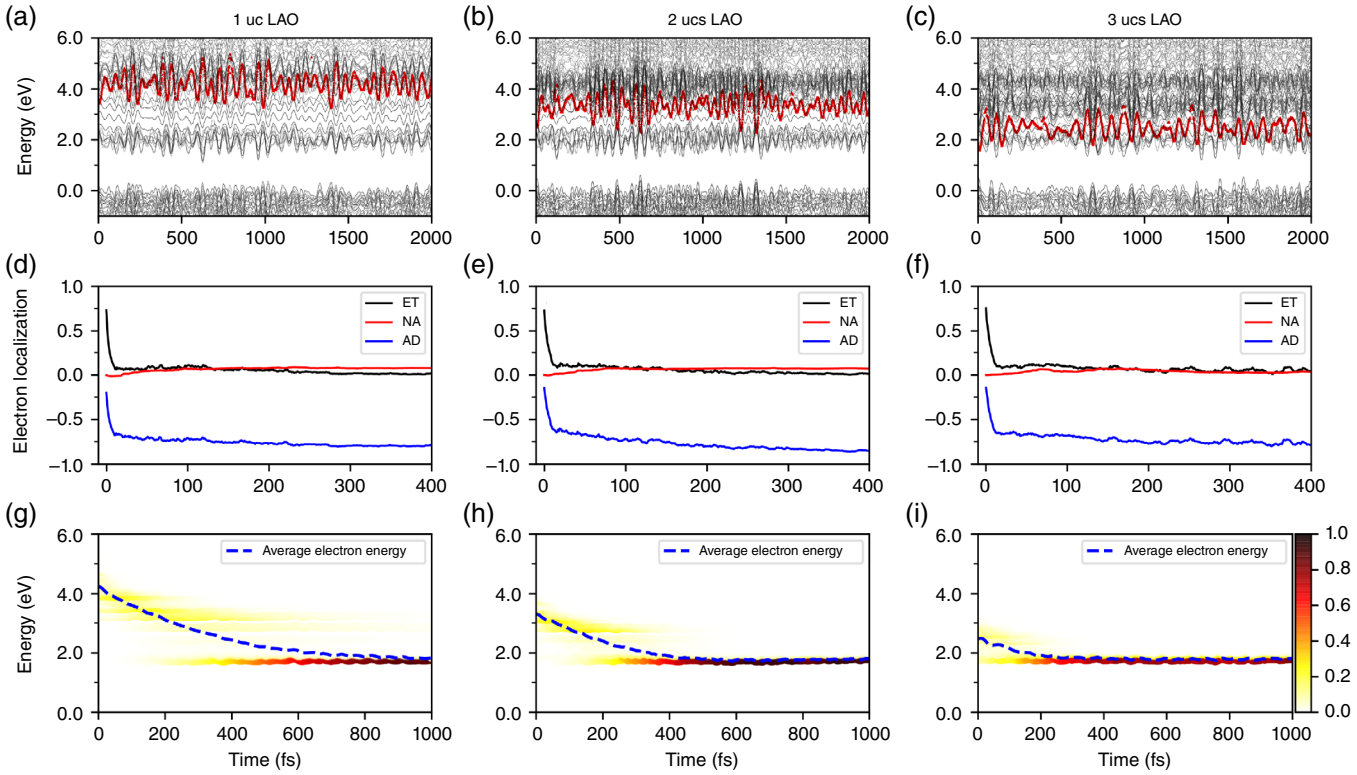

FIGURE 4 Charge transfer dynamics of solvated electron of 1ML H_2O adsorbed on *p*-type of LAO/STO with 1–3 ucs LAO. (a–c) Time-dependent energy state evolution. The black (red) lines represent the energy levels contributed by LAO/STO (SEBM of H_2O). (d–f) Time-dependent electron localization projected onto the H_2O layer and *p*-type LAO/STO substrate. The total electron transfer (labeled as ET with black line) and the AD and NA contributions (blue and red lines) to the charge transfer are also plotted. (g–i) Time-dependent electron energy change. The energy of VBM is set as reference in panel (a–c) and (g–i). (Reprinted with permission from Reference 95. Copyright 2018 American Chemical Society)

dynamics are dominated by the AD charge transfer mechanism due to the multiple crossings between the solvated electron states with the LAO bulk states, showing similar behavior with the reverse hole transfer from CH_3OH to TiO_2 surface. Photocatalytic process is generally difficult to take place within such a short timescale. Yet when the LAO thickness reaches 4 ucs, the SEBM becomes the CBM of the whole system and the lifetime of solvated electrons can be much longer. When LAO thickness reaches 8 ucs, the SEBM can even be occupied. This method of tuning the solvated electron state energy at aqueous/oxide surface is proposed to be generally applicable for different polar–nonpolar systems as well as the ferroelectric systems as the electric field can exist in such systems.

5 | SUPERATOM MOLECULAR ORBITAL AS AN INTERFACIAL CHARGE SEPARATION STATE

In the process of solar energy conversion, including the photocatalysis and photovoltaics, the energy loss during hot carrier cooling through e–p coupling is an important factor which can limit the efficiency of solar energy conversion.[96] A charge separation state, which can extract the hot carriers before they cool, can be used to enhance the efficiency of solar energy conversion. Usually such charge separation state can also produce an enhanced photovoltage and reduce the e–h recombination.[97,98] In such a charge separation process, it is required that the interfacial charge transfer across the contacts must be faster than the rate of carriers cooling.[99] In spite of numerous investigations on the charge separation mechanism at the hybrid solar cell interfaces,[98,100–110] this is still one of the most important and challenging problems in this field. Using NAMD simulations, Guo et al.[111] proposed that the superatom molecular orbitals (SAMOs) and the nearly free electron (NFE) states of carbon nanostructures which were initially discovered by Feng et al.,[112] is an ideal media for interfacial charge separation.

5.1 | Phonon bottleneck in hot electron relaxation induced by SAMO

Distinct from the well-known π^* states in fullerenes, SAMOs are bound to the central screening potential of fullerenes instead of individual C atoms, showing NFE character. The NAMD simulations show that the lifetime of the hot electron on SAMO showing character analogous to *s* orbital (*s*-SAMO) is much longer comparing to π^* orbitals. As shown in Figure 5a, the hot

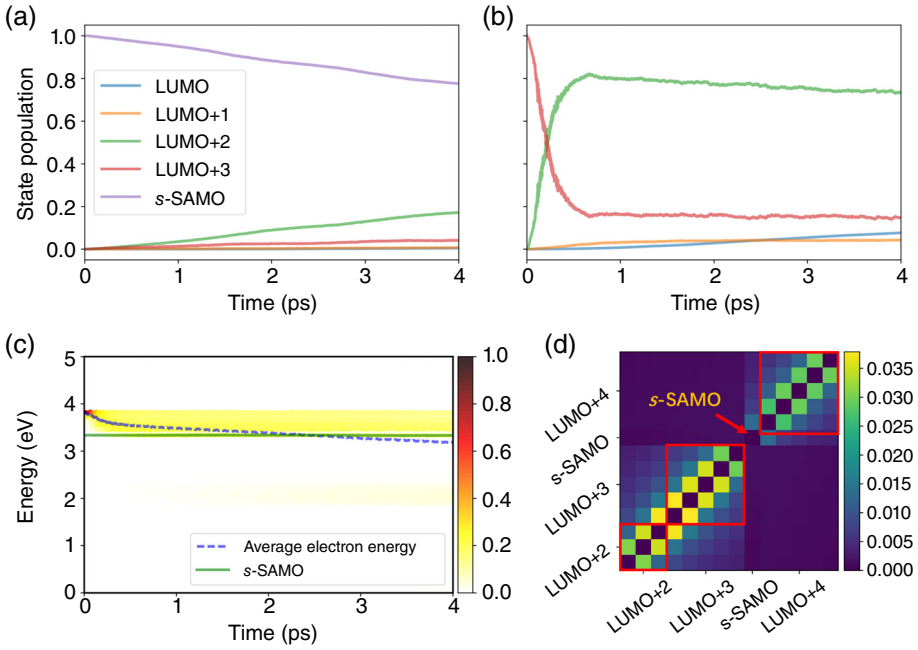

FIGURE 5 The time-dependent state population evolutions for LUMO to *s*-SAMO where the hot electron is initially excited at (a) *s*-SAMO or (b) or LUMO +3, respectively. (c) The time-dependent averaged energy evolution for hot electron initiated from a state 0.5 eV above the SAMO. The color strip indicates the hot electron distribution on different energy states and the dashed line represents the averaged hot electron energy. (d) The NACs among different states from LUMO+2 to LUMO+4 (due to the degeneracy, LUMO+2, +3 and +4 are framed by red box). (Reprinted with permission from Reference 111. Copyright 2018 American Chemical Society)

electron on *s*-SAMO decays by around 20% in 0.5 ps. By contrast, for LUMO+3, which is a typical π^* orbital, the hot electron decays by more than 80% within 0.5 ps (Figure 5b). By fitting the decay to an exponential function, the lifetime of *s*-SAMO can be estimated to be around 20 ps, which is 40 times longer than that of lowest unoccupied molecular orbital (LUMO)+3. Figure 5c shows that when a hot electron is generated at 0.5 eV above the *s*-SAMO, it will decay to *s*-SAMO within 1 ps. After that, the subsequent relaxation is much slower. One can see that *s*-SAMO behaves exactly as a "bottleneck" for hot electron cooling.

The slowdown of the hot electron cooling of *s*-SAMO can be understood using the "phonon bottleneck" concept.[113–117] Previous studies proposed that the energy gap between different levels is important for phonon bottleneck.[117–121] Here the phonon bottleneck induced by *s*-SAMO is due to two factors: the energy gap as large as 1 eV below *s*-SAMO and the weak e–p coupling. In agreement with previous studies, Guo et al.[111] proved that *s*-SAMO of C_{60} has weak e–p coupling due to the diffusive NFE character. As shown in Equation (3), the small e–p coupling induces a small NAC between *s*-SAMO and other states, which can be seen in Figure 5d. And the reduction of NAC will directly suppress the charge relaxation between different states.

5.2 | Fast interfacial charge transfer induced by SAMO

Besides the phonon bottleneck for the internal hot electron cooling, the *s*-SAMO can also induce the fast interfacial charge transfer. Guo et al. chose MoS_2 as a substrate to couple with C_{60} due to its important applications in photonics and photovoltaics.[78,122–124] The time-dependent energy evolution of electronic states of C_{60}/MoS_2 are shown in Figure 6a. One can see that during the MD simulation, the MoS_2 levels cross *s*-SAMO frequently. The hybridization between *s*-SAMO and MoS_2 is significant when their energies are close because of the diffuse NFE character of *s*-SAMO and the charge transfer induced by the AD mechanism is enhanced. As shown in Figure 6b, the charge transfer from *s*-SAMO to MoS_2 happens within 200 fs, which is two orders of magnitude faster than the hot electron cooling from *s*-SAMO.

To conclude, by performing time-dependent ab initio NAMD simulations on prototypical system C_{60}/MoS_2, it was shown that *s*-SAMO of C_{60} behaves as an important charge separation state. Due to its NFE properties, on one hand the *s*-SAMO of C_{60} generates a phonon bottleneck for the internal electron relaxation. On the other hand, it induces significant hybridization at C_{60}/MoS_2 interface and the fast interfacial charge transfer. Since the NFE-like states generally exist in different carbon nanostructures like fullerenes, graphene and carbon nanotubes, Guo et al.[111] proposed that such a conclusion can be extended to different interfaces constructed by carbon nanostructures.

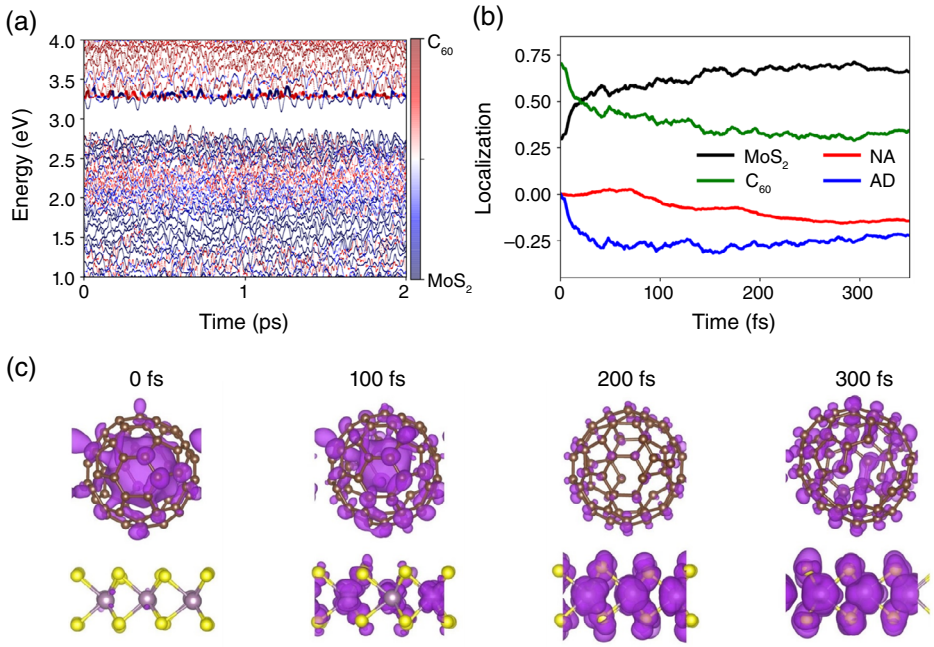

FIGURE 6 (a) The time evolutions of the energy states of C_{60}/MoS_2 in NAMD simulations. The color strip indicates the state distribution on C_{60} and MoS_2. The *s*-SAMO state is marked using thicker line. (b) Time-dependent electron transfer from *s*-SAMO of C_{60} to MoS_2 and the NA/AD contribution. (c) Snapshots of the orbital distribution in the NAMD simulation at 0, 100, 200 and 300 fs. (Reprinted with permission from Reference 111. Copyright 2018 American Chemical Society)

6 | ULTRAFAST CHARGE TRANSFER AT VAN DER WAALS HETEROSTRUCTURE INTERFACE

The vdW heterostructures formed by 2D materials have important applications in optoelectronics and solar energy conversion. The effective charge separation is a key factor for the solar energy conversion efficiency. Because of the weak interaction at the vdW heterostructure interface, fast charge transfer was not expected. However, contrary to the common expectation, recent experimental works observed the ultrafast charge transfer dynamics occurring at the interface of vertically stacked transition-metal dichalcogenide (TMD) heterostructure bilayers with type-II band alignment.[3,13,125–127] Therefore, it is urgent and essential to understand such ultrafast charge transfer dynamics at TMD interfaces. Zheng et al. used ab initio NAMD to investigate the photogenerated carrier dynamics at MoS_2/WS_2 and $MoSe_2/WSe_2$ interfaces.

6.1 | Phonon-assisted hole transfer at MoS_2/WS_2 interface

Zheng et al.[64] first investigated the photogenerated hole transfer dynamics at MoS_2/WS_2 interface. The time-dependent hole population and averaged hole energy at the MoS_2/WS_2 interface are shown in Figures 7 and 8, respectively. By comparing Figures 7 and 8, the hole dynamics pathway in momentum space can be determined. Different stacking effects were considered in Reference 64, where two of the most stable stacking structures C7 and T are discussed. Usually the hole is initially generated at *K* point in MoS_2 ($MoS_2@K$). It is very interesting to see from Figure 7b that for T stacking the hole dynamics occur on both fast and slow time scales. The fast component corresponds to a interlayer hole transfer from $MoS_2@K$ to $WS_2@\Sigma$ within 20 fs, whereby the hole distribution on WS_2 increases from 10% to 55%. After this primary transfer is completed, there is a slow component which involves mainly an intralayer hole relaxation from $WS_2@\Sigma$ to $WS_2@K$ within 600 fs and the hole localization converges to 70%. In contrast, the ultrafast interlayer hole transfer is not found for C7 stacking. In this case, the hole transfer directly from $MoS_2@K$ to $WS_2@K$, as shown in Figure 7a.

If the electron phonon scattering is considered, the hole transfer can also happen at Γ point. Interestingly, in this case, the ultrafast interlayer hole transfer is found in C7 stacking. There are also two components in this hole transfer process. First, there is an ultrafast interlayer hole transfer from $MoS_2@\Gamma$ to $WS_2@\Sigma$ with the hole distribution on WS_2 increasing from 40% to 60% within 20 fs. Then a slow intralayer hole relaxation within 300 fs follows, whereby the hole distribution on WS_2 converges to 70%. One can see that for both C7 and T stacking, the ultrafast interlayer hole transfer at 20 fs can be observed.

Analysis shows that for both C7 and T stacking the ultrafast interlayer hole transfer process is dominated by the AD charge transfer mechanism. This is due to the many crossings between the donor and the acceptor states along the MD

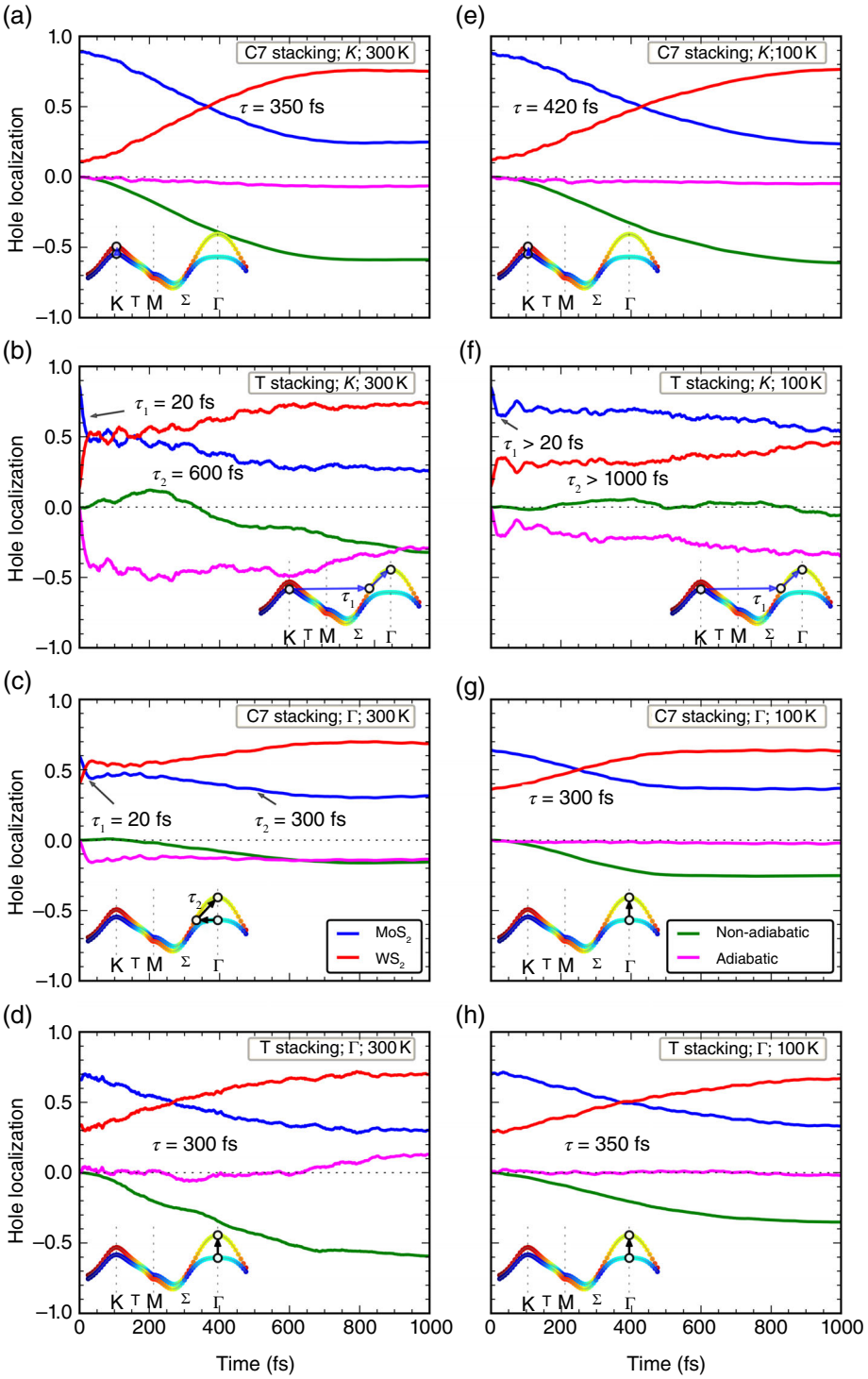

FIGURE 7 Time-dependent spatial hole localization at the *K* and Γ points for the C7 and T stackings at 300 K (*K* point (a, b), Γ point (c, d)) and 100 K [*K* point (e, f), Γ point (g, h)]. The major hole relaxation routes in momentum space are schematically shown in the insets. The AD and NA contributions to the hole dynamics are shown, where their sum indicates the decrease of hole localization within the MoS_2 layer. (Reprinted with permission from Reference 64. Copyright 2017 American Chemical Society)

trajectory. By contrast, the slow interlayer hole transfer processes (C7 stacking at *K* point and T stacking at Γ point as shown in Figure 7a,d) are almost completely promoted by the NA charge transfer mechanism.

Ultrafast interlayer hole transfer provoking by the AD mechanism suggests that this process is significantly sensitive to phonon excitation. This point was verified by temperature dependent simulations. As shown in panels a–d in Figure 9, the NAMD simulation at 100 K shows that, by decreasing the temperature, the phonon occupation and the energy oscillation amplitude will be reduced. When the nuclear motion is decreased, there are almost no crossings between the donor and acceptor states and the AD charge transfer will be suppressed as shown in Figure 7e,f. By contrast, the NA charge transfer does not

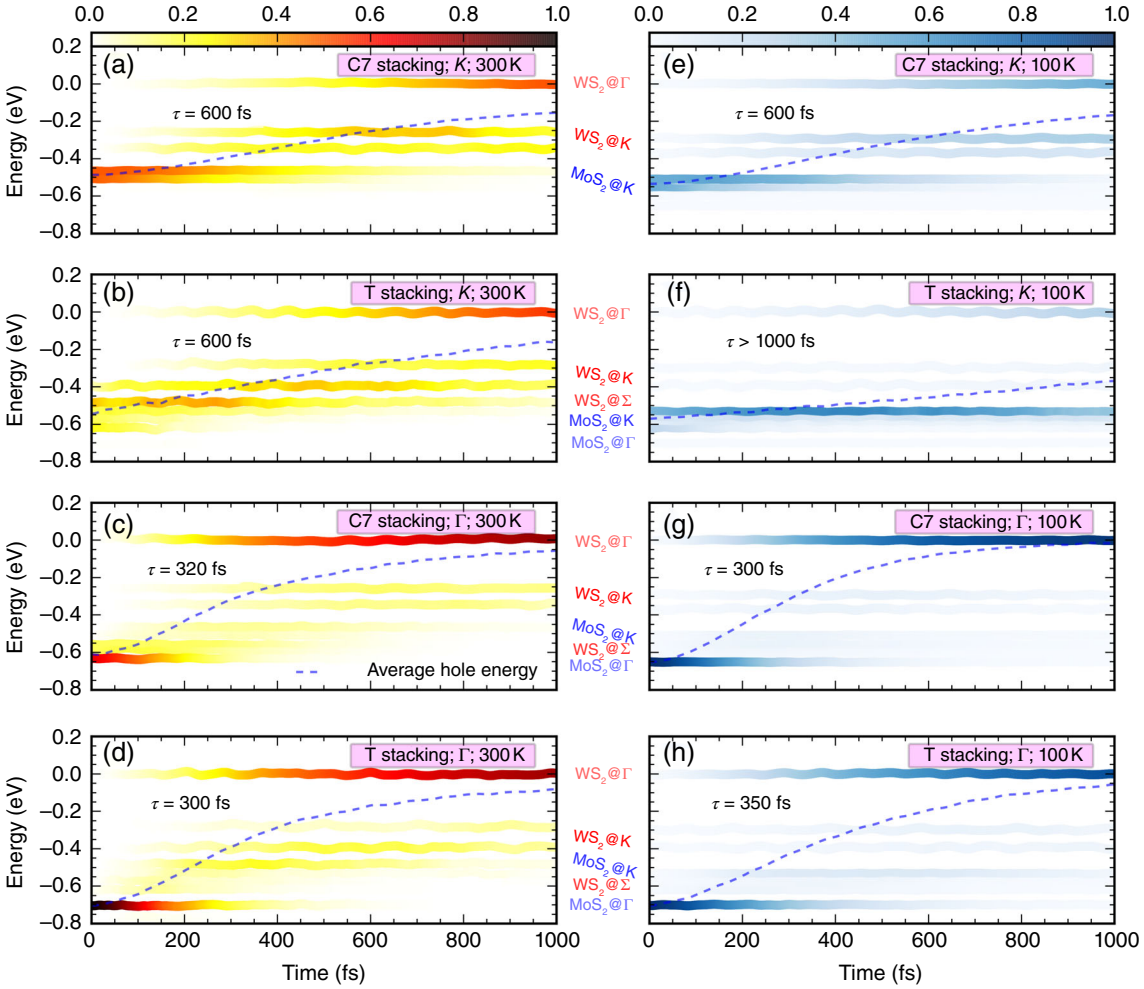

FIGURE 8 Time-dependent hole energy change at the *K* and Γ points for the C7 and T stacking at 300 K [*K* point (a, b), Γ point (c, d)] and 100 K [*K* point (e, f), Γ point (g, h)]. The color strips indicate the hole distribution on different energy states and the dashed line represents the averaged hole energy. The energy reference is the average VBM energy. (Reprinted with permission from Reference 64. Copyright 2017 American Chemical Society)

change significantly. Furthermore, FT spectra have been used to determine which phonon modes are essential for the charge transfer. One can see from Figure 9e–h that the donor and acceptor states are coupled with the intralayer out-of-plane A_1 optical phonon at ~400 cm^{-1}, a LA mode at ~200 cm^{-1}, and the optical out-of-plane interlayer breathing mode at ~35 cm^{-1}. The corresponding vibrational periods are 83, 166 and 953 fs, respectively. The timescale of the ultrafast interlayer charge transfer is 20 fs, which is approximately one quarter cycle of the A_1 mode, suggesting that A_1 mode is the essential phonon mode which promotes the ultrafast charge transfer. One should note, however, that the temperature-dependent results were not observed in the experimental measurements. Zheng et al.[64] proposed that this might be due to the lack of quantum nuclear effects in the simulation.

In order to estimate the nuclear quantum effects, quantum and classical kinetic energy of the phonon system were inspected, respectively. The quantum kinetic energy (K_Q) is defined as

$$K_Q \approx \frac{\left(\frac{\hbar\bar{\omega}}{2} + \frac{\hbar\bar{\omega}}{exp(\hbar\bar{\omega}/k_B T)-1}\right)}{2} \tag{7}$$

where $\bar{\omega}$ is averaged phonon frequency, which is 250 cm^{-1} for MoS_2/WS_2. In contrast, the classical kinetic energy (K_C) can be estimated as:

$$K_C \approx \frac{k_B T}{2} \tag{8}$$

In Figure 10 K_Q and K_C and their ratio K_C/K_Q are plotted out. One can see that the change of K_C/K_Q has a turning point between 100 and 150 K, suggesting that below 100 K the nuclear quantum effects increase distinctly. It can be seen that K_Q (T = 100 K) ≈ K_C (T = 210 K), suggesting that to simulate an experimental measurement at 100 K, one needs to perform

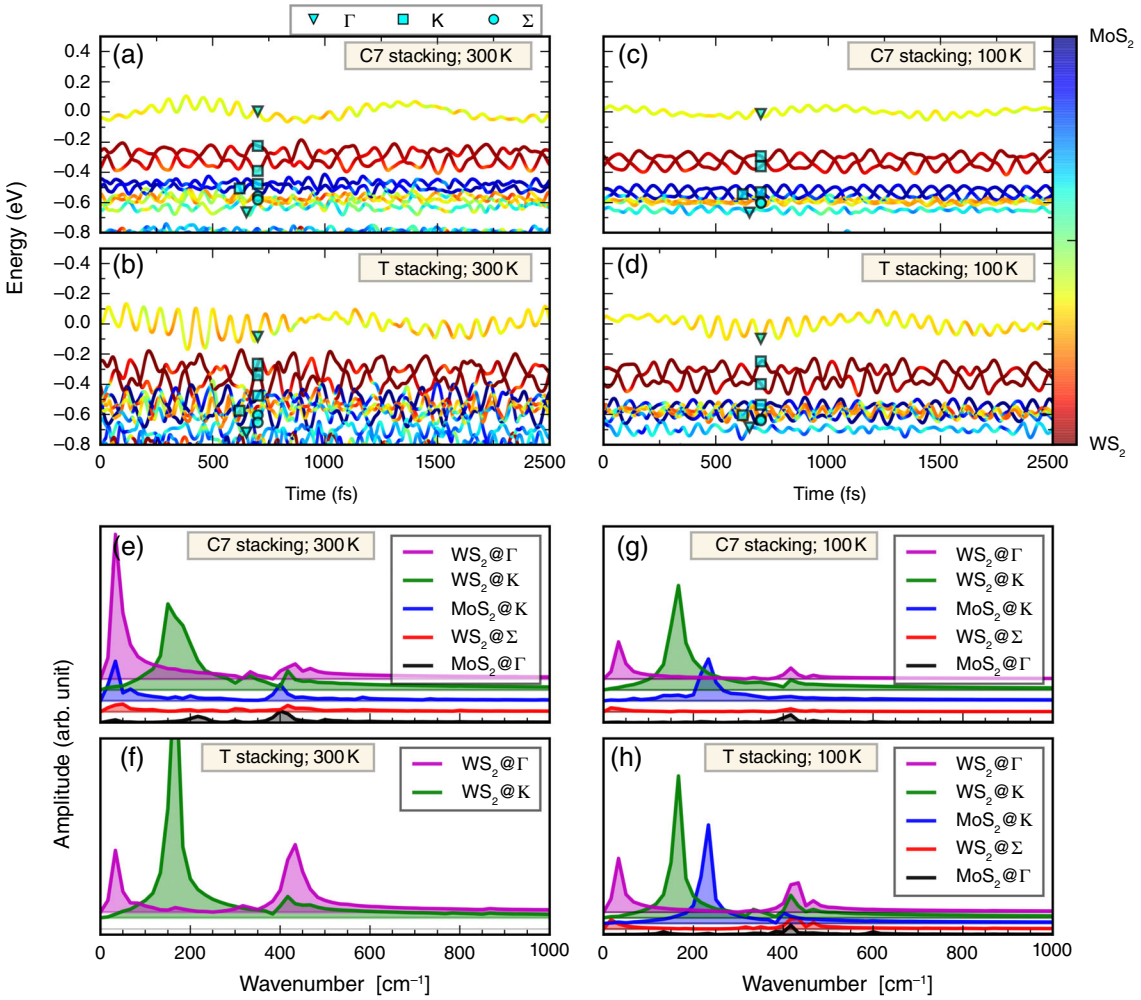

FIGURE 9 Time evolutions of the energy states near VBM (a–d) and their FT spectra (e–h) for C7 and T stackings at 300 and 100 K. The energy reference in (a–d) is the average VBM energy and the color map shows the hole localization. The triangle, square and circle in (a–d) indicate the momentum of different energy states. (Reprinted with permission from Reference 64. Copyright 2017 American Chemical Society)

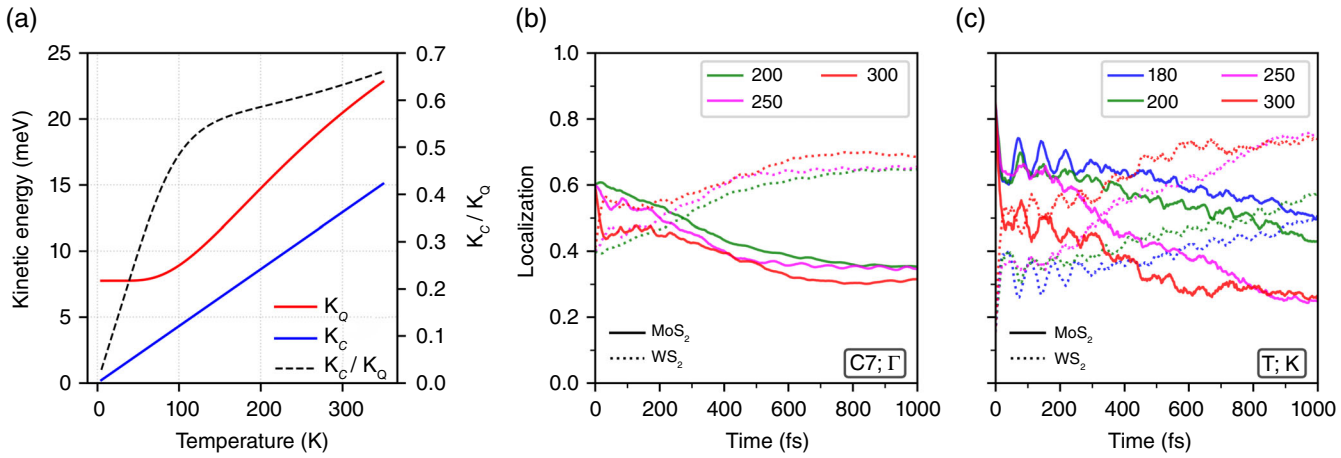

FIGURE 10 (a) Temperature dependence of K_Q and K_C. The ratio K_C/K_Q is also plotted. (b, c) Time-dependent spatial hole localization at different temperatures (300, 250 and 200 K for C7 stacking at Γ point (b) and 300, 250, 200 and 180 K for T stacking at *K* point (c)) (Reprinted with permission from Reference 64. Copyright 2017 American Chemical Society)

a simulation at around 210 K. Further, K_Q ($T = 0$ K) ≈ K_C ($T = 180$ K), implying the existence of zero-point energy. It suggests that a temperature of 180 K is still needed to simulate the measurement at 0 K. To make a better comparison with experimental results, more detailed temperature-dependent simulations for C7 and T stackings at 300, 250, 200 and 180 K were performed. The results are shown in Figure 10b,c. For C7 stacking, the phonon-assisted ultrafast charge transfer happens at

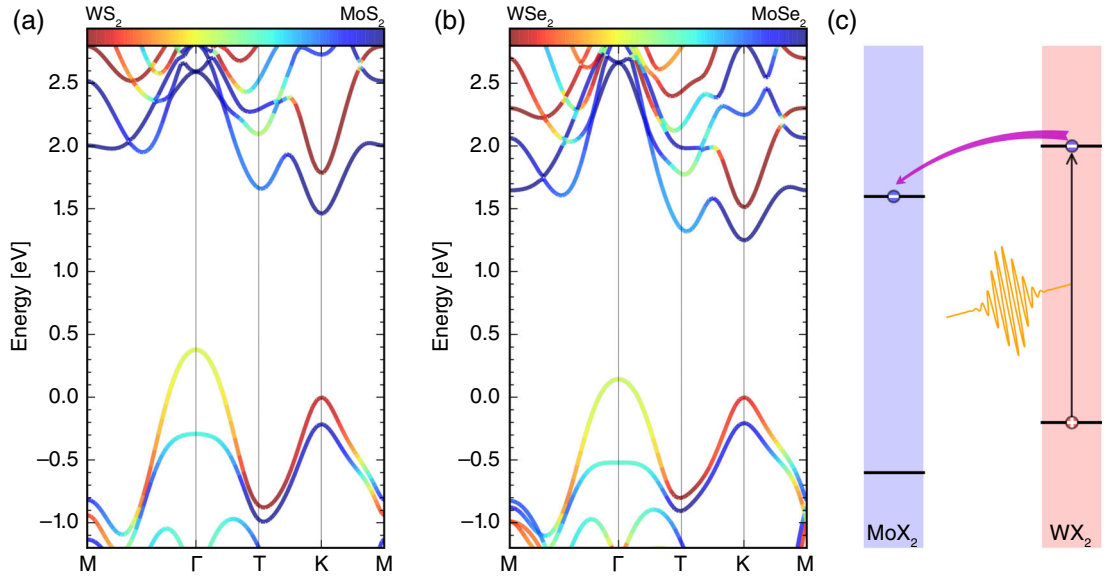

FIGURE 11 Band structures and orbital spatial distributions of (a) MoS_2/WS_2 and (b) $MoSe_2/WSe_2$ heterostructures. The energy of $WX_2@K$_VB is set to zero. The color strip indicates the localization of the states. The photoexcitation and the initial electron distribution are indicated in (a, b). The schematic of electron transfer in TMD heterostructure is shown in (c). (Reprinted with permission from Reference 128. Copyright 2018 American Physical Society)

300 and 250 K, but disappear at 200 K, suggesting the critical temperature for ultrafast hole transfer is within 200–250 K range in the classical regime; the corresponding temperature falls in 90–135 K range if quantum nuclear effects are included. For T stacking, the ultrafast process still happens when the temperature is decreased to 180 K, implying that such an ultrafast process can be observed even near zero temperature.

6.2 | Phonon-coupled charge oscillation at $MoSe_2/WSe_2$ interface

As has been discussed above, in the investigation of charge transfer dynamics at MoS_2/WS_2 interface, Zheng et al.[128] proposed that the ultrafast charge transfer is provoked by the phonon excitation through e–p coupling. To further understand how the e–p coupling affect the interfacial charge transfer at TMD interface, Zheng et al. performed further studies on the photogenerated electron transfer at $MoSe_2/WSe_2$ and compared the results with those of MoS_2/WS_2. The two TMD heterostructures have similar band structures as shown in Figure 11a,b. The photogenerated electron transfer process is illustrated in Figure 11c. The donor and acceptor states are $WX_2@K$ (X = S, Se) and $MoX_2@K$, respectively. The $MoX_2@T$ state may also be involved in the charge transfer process. The orbital distribution of $WX_2@K$, $MoX_2@T$ and $MoX_2@K$ are plotted in Figure 11a,b.

MoS_2/WS_2 and $MoSe_2/WSe_2$ were chosen as a group to compare because they have similar band structures yet distinct phonon frequencies and e–p couplings due to the different chalcogen elements. The difference of the phonon frequencies and e–p coupling for $MoSe_2/WSe_2$ and MoS_2/WS_2 can be understood from the e–p coupling induced oscillation of the KS energies at 300 and 100 K and their FT spectra shown in Figure 12a–d. First, because more phonons are thermally excited at 300 K than those at 100 K, the energy oscillation at 300 K is stronger for both MoS_2/WS_2 and $MoSe_2/WSe_2$. Next, the energy oscillation amplitudes of $MoSe_2/WSe_2$ are always larger than MoS_2/WS_2 at the same temperature. The FT transform of the time-dependent eigen-energies of $MoX_2@K$, $MoX_2@T$ and $WX_2@K$ are shown in Figure 12e–h. For MoS_2/WS_2, the major peak appears at around 400 cm^{-1} whereby it redshifts to 230 cm^{-1} in $MoSe_2/WSe_2$. The major peak in both systems can be assigned to be the A_1 mode by comparing with the Raman scattering measurements and first-principles calculations.[3,129–132] The redshift of A_1 mode in $MoSe_2/WSe_2$ is due to the different chalcogen masses and chemical interactions. At the same temperature, because A_1 mode in $MoSe_2/WSe_2$ is much softer than that in MoS_2/WS_2, more phonons will be excited in $MoSe_2/WSe_2$, resulting in the stronger energy oscillations.

The electron transfer processes at the interfaces of $MoSe_2/WSe_2$ and MoS_2/WS_2 were studied using NAMD simulations. The results are summarized in Figure 13. The time-dependent charge localization and averaged electron energies for $MoSe_2/WSe_2$ system at 300 K are shown in Figure 13a–c. At 300 K, charge localization on WSe_2 decreases from 90% to 10% with the energy of excited electron relaxing to CBM within 1,000 fs. The interesting point is that during the initial 400 fs, the interlayer charge oscillation occurs with the same period of the A_1 phonon mode. In the momentum space, this corresponds to an intervalley charge transfer from $WSe_2@K$ to $MoSe_2@T$. It is followed by an intervalley charge relaxation from $MoSe_2@T$ to $MoSe_2@K$. It was proposed that the A_1 phonon mode plays an important role in these intervalley electron transfer and

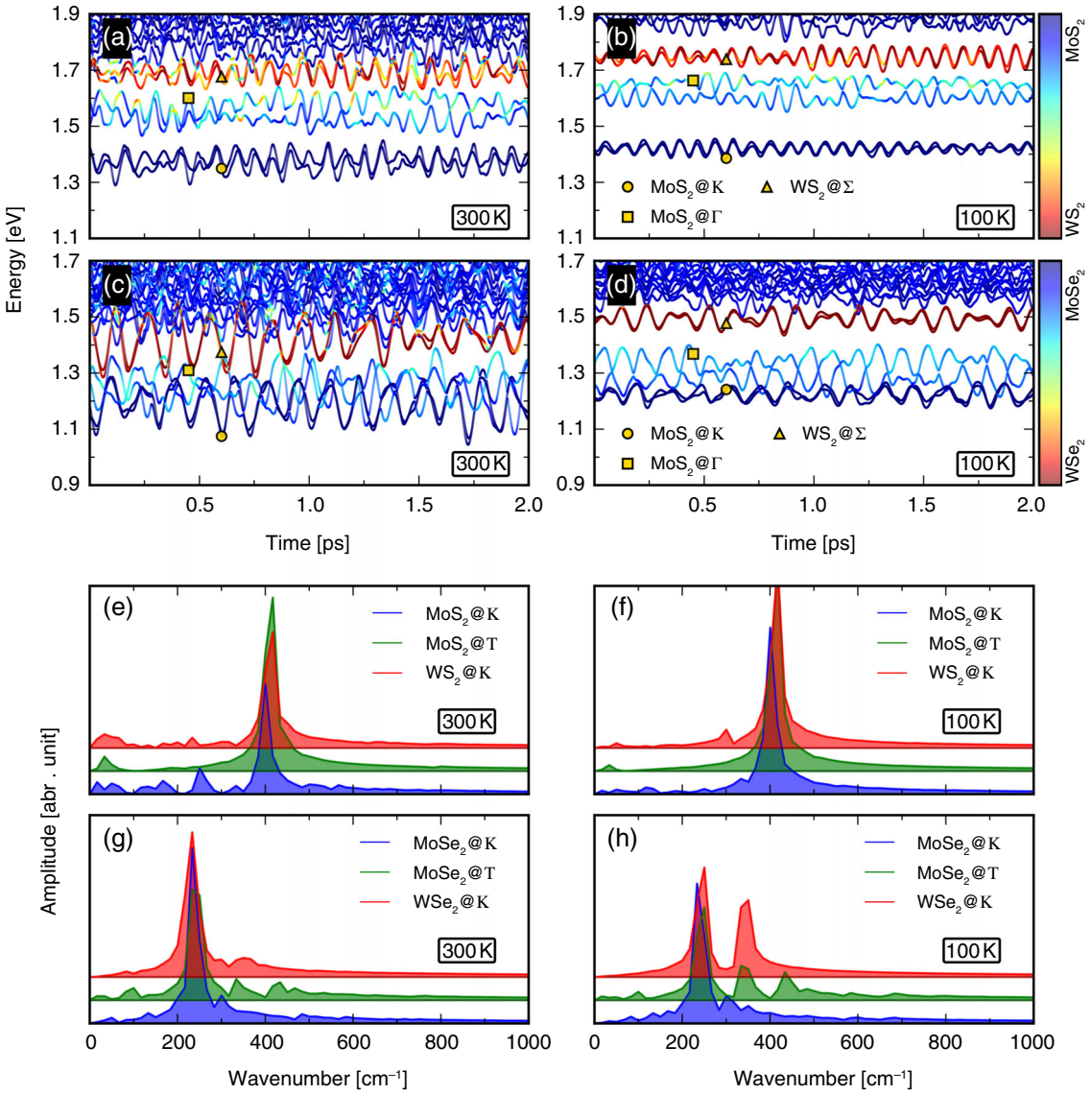

FIGURE 12 Time evolutions of the energy states near CBM (a–d) and FT spectra of the selected states (e–h) of MoX_2/WX_2 (X = S, Se) heterostructures at 300 and 100 K. The energy reference in (a–d) is the averaged energy of $WX_2@K\_VB$, and the color map shows the orbital localization. (Reprinted with permission from Reference 128. Copyright 2018 American Physical Society)

relaxation.[128] By contrast, the excited electron transfer dynamics at MoS_2/WS_2 interface show distinct properties. As can be seen from Figure 13d, in 1 ps the electron localization on WS_2 decreases from 75% to nearly 10% at 300 K. During this process there is no charge oscillation. Further analysis shows that although the electron transfer pathway is still from $WS_2@K$ to $MoS_2@T$ and finally to $MoS_2@K$, the NA charge transfer mechanism is the major component, indicating that the electron tends to tunnel between the donor and acceptor states instead of oscillate coherently with the phonons.

The significantly different charge transfer dynamics behaviors between MoS_2/WS_2 and $MoSe_2/WSe_2$ can be interpreted from two insights. First, the A_1 mode in $MoSe_2/WSe_2$ has a relatively low frequency (230 cm^{-1}). Therefore, there can be sufficient phonon excitation at 300 K, leading to the phonon-coupled charge oscillation. On the contrary, in MoS_2/WS_2 the frequency of A_1 mode is as high as 400 cm^{-1}, which makes the phonon excitation at 300 K to be more difficult and thus the phonon-coupled charge transfer is suppressed. Second, for MoS_2/WS_2 system, the NAC elements between the donor ($WS_2@K$) and acceptor ($MoS_2@T$) are relatively large due to the smaller energy difference comparing with $MoSe_2/WSe_2$. Owing to the weak phonon excitation and large NAC elements, in MoS_2/WS_2 the charge transfer is dominated by the NA mechanism, whereby the direct charge tunneling is in the leading role. By contrast, in $MoSe_2/WSe_2$, the sufficient phonon excitation and small NAC elements induce the coherent charge oscillation with A_1 phonons.

The ab initio NAMD investigations by Zheng et al. indicate that the excitation of the intralayer A_1 phonon mode is very important to understand the interlayer charge transfer dynamics in TMD heterojunctions measured by experiments. In MoS_2/WS_2, it was proposed that the ultrafast charge transfer is provoked by the A_1 mode excitation. Furthermore, in $MoSe_2/WSe_2$,

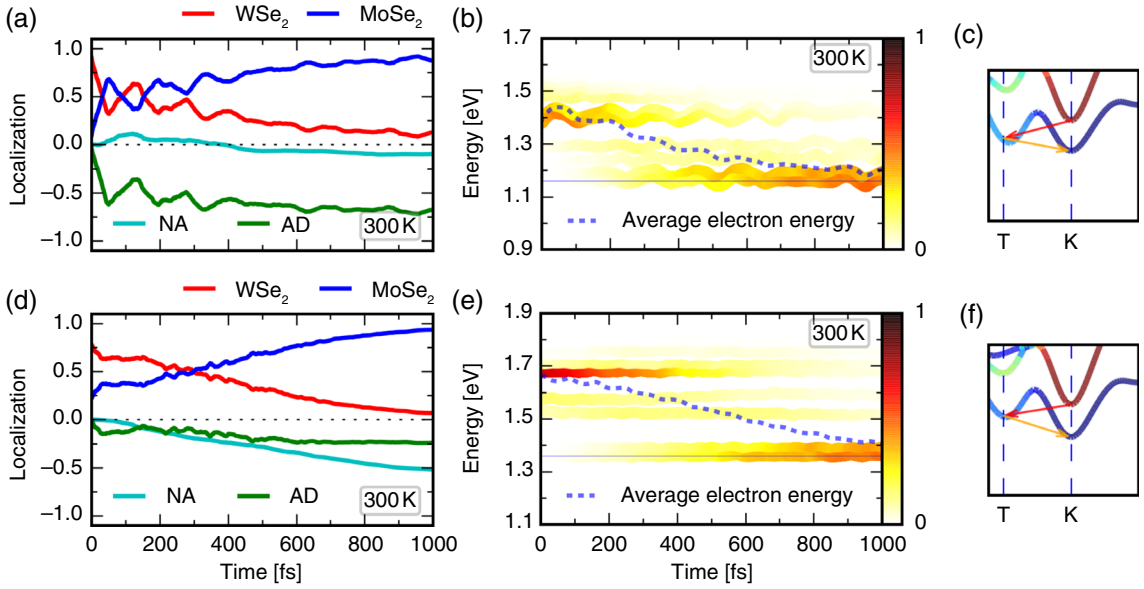

FIGURE 13 Nonadiabatic molecular dynamics results of $MoSe_2/WSe_2$ and MoS_2/WS_2 at 300 K, respectively. (a, d) Time-dependent electron spatial localization. (b, e) Time-dependent electron energy change. (c, f) Schematics of the electron relaxation route in the momentum space. (Reprinted with permission from Reference 128. Copyright 2018 American Physical Society)

where the A_1 phonon mode can be more sufficiently excited, Zheng et al. proposed a phonon-coupled electron oscillation can be achieved. The results that phonon excitation plays crucial role for charge transfer based on MoS_2/WS_2 and $MoSe_2/WSe_2$ can be extended to other TMD heterostructures. The phonon excitation and e–p coupling can be tuned by different experimental techniques or environments. For example, changing the substrate or applying external stress can change the phonon frequencies and e–p coupling strength. Furthermore, recent phonon pumping techniques using infrared light make it possible to excite selected resonant lattice phonons. Therefore, the phonon couple charge transfer is possible to be controlled, which may have important applications in the design of 2D optoelectronic devices and solar energy conversion systems.

It should also be noticed that the charge transfer dynamics at TMD interface have also been investigated by other theoretical works. Wang et al. used Erhenfest NAMD based on TDDFT (TDAP code) to investigate the hole transfer process in MoS_2.[133] In their work they also found the A_1 and LA modes play important role in the MD. They found the hole transfer from MoS_2 to WS_2 happen with a timescale of 100 fs, accompanying charge oscillation between the two layers. They attribute such charge oscillation is coupled with the dipole moment. Ji et al. studied the same process using the same Erhenfest NAMD method collaborating with time-resolved optical pump-probe spectroscopy.[125] For different layer stackings, the hole transfer timescale varies from 180 to 1,500 fs, providing different charge transfer channels. They proposed that in the experiments the hole transfer occurs through the fast channel. Here one can see that the NAMD simulations based on Erhenfest and surface hopping schemes give different timescales (varying from 20 to 1,500 fs) for hole transfer at MoS_2/WS_2 interface. In Erhenfest simulations the charge oscillations are proposed,[125,133] while in surface hopping simulation there are a fast and a slow component contributed by the AD and NA mechanisms.[64] The surface hopping NAMD results do not depend on the stacking of TMD layers,[64] which in agreement with the experimental results.[3] However, the temperature dependence proposed by surface hopping NAMD is not observed in the experiments. In addition, the exciton binding plays an important role in 2D TMD systems and it is not included in the current surface hopping NAMD simulations. Yet in the Erhenfest NAMD simulation it is included in a mean-field manner. In the future, we propose to develop new aspects in Hefei-NAMD to include the exciton binding and quantum nuclear effects and will revisit the topic of charge transfer dynamics at 2D TMD interface.

7 | ELECTRON–HOLE RECOMBINATION IN DOPED SEMICONDUCTOR

Besides the charge transfer dynamics at different interfaces, ab initio NAMD simulations can also be used to investigate the photogenerated e–h recombination dynamics. Zhang et al. chose a wide band gap semiconductor TiO_2, which is one of the most intensively studied photocatalyst, as a prototypical system to study how the cation and anion doping affect the e–h recombination rate.[134] Different cation doping in wide band gap semiconductors is proposed to be an effective route to reduce the band gap, improve the photon energy absorption and enhance the solar energy conversion efficiency.[135–139] However, it may also introduce e–h recombination centers which will affect the lifetimes of the photogenerated electrons and holes. Based

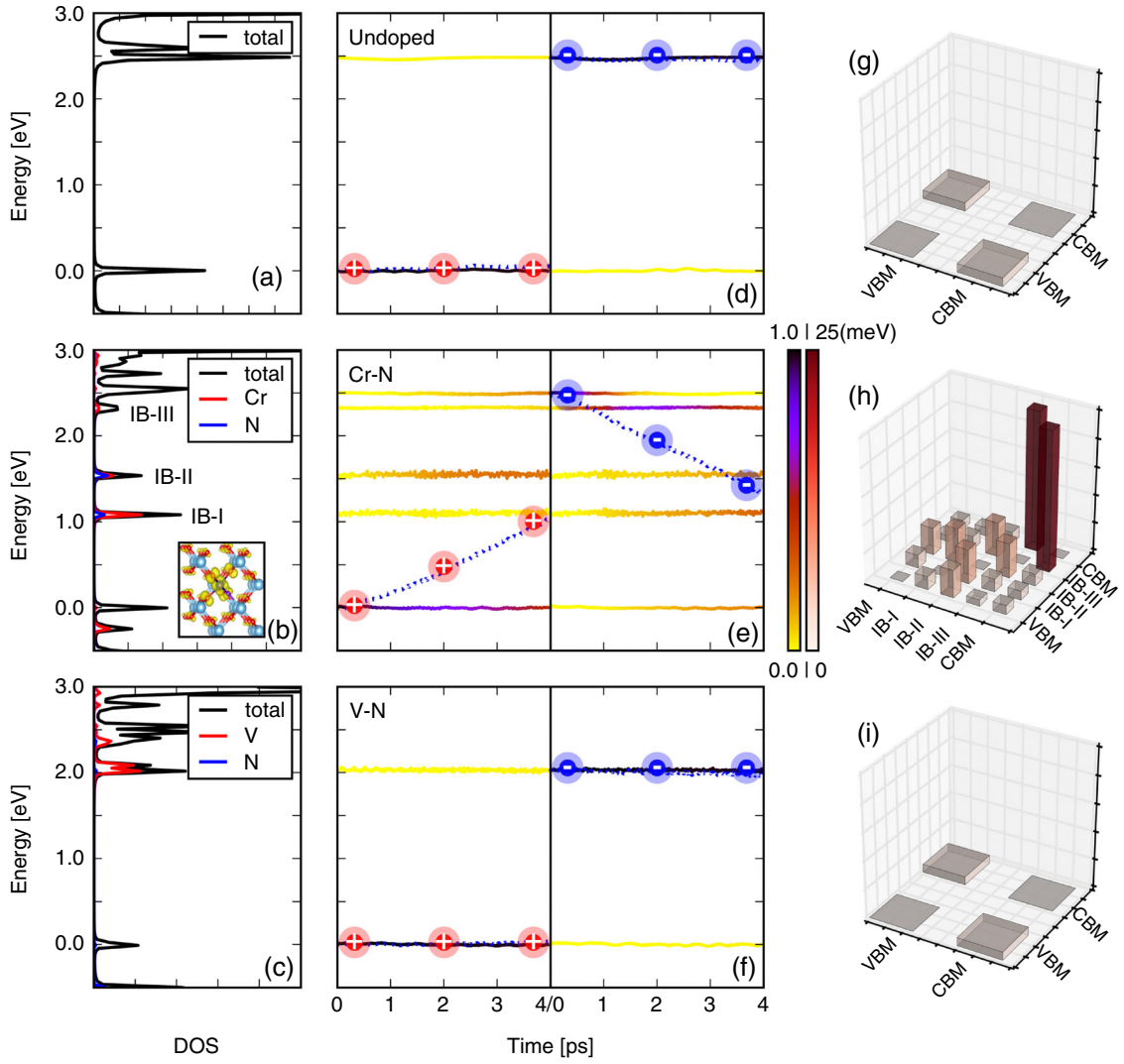

FIGURE 14 The electronic structures and the time-dependent electron–hole (e–h) dynamics in undoped, Cr—N- and V—N-doped TiO_2. (a–c) The total and partial density of states. (d–f) The averaged time-dependent e–h energy relaxation at 300 K. The color strip indicates the e–h distribution on different energy states and the dashed line represents the averaged e–h energy. The energy reference is the average VBM energy. (g–i) The averaged NAC elements in undoped, Cr—N- and V—N-doped TiO_2 at 300 K. The inset in (b) shows the spatial distribution of the excess charge induced by Cr—N codoping, in which the Ti, O, Cr and N atoms are marked by large light blue, small red, large deep blue and small purple balls, respectively. (Reprinted with permission from Reference 134. Copyright 2018 American Chemical Society)

on NAMD simulations, Zhang et al. proposed that the localization of impurity-phonon modes (IPMs) is the key factor for the e–h recombination rate.[134]

Among these doping schemes in TiO_2, the *n–p* codoping by both anions and cations was proposed to have better thermodynamic stability compared with monodoping.[138,139] Noncompensated Cr—N and compensated V—N codoping were chosen for contrast since V and Cr are neighbors in the periodic table of elements. As shown in Figure 14a–c, Cr—N doping introduces three intermediate bands (IBs). Among them, there are two bands (labeled as IB-I and IB-II) contributed by the Cr—N impurities in the middle of band gap and one hybridized band (IB-III) contributed by both Cr—N and TiO_2 close to CBM. In contrast, the compensated doping V—N does not introduce IBs in the band gap of TiO_2. Instead, it only narrows the band gap by downward and upward shifting of CBM and VBM. As shown in Figure 14c, VBM of V—N-doped TiO_2 is a hybridized state contributed by O and N 2*p* orbitals, and CBM is mostly contributed by the doping V 3*d* orbital.

The CBM and VBM of Cr—N- and V—N-doped TiO_2 were chosen as the initial states for the electron and hole relaxation. The undoped TiO_2 was also investigated as a contrast. Figure 14d–f shows the time-dependent population and averaged energies of excited electron and hole in these three systems. The e–h recombination behavior in V—N-doped TiO_2 is similar with that in undoped TiO_2, while it is significantly different in Cr—N-doped TiO_2. For V—N-doped and undoped TiO_2, the e–h recombination events can be hardly seen within 4 ps, suggesting that the e–h recombination timescale is much longer than the ps magnitude. In this case the NAMD simulation in several ps can barely obtain the accurate e–h recombination timescale. It can be estimated to be around 0.5 ns by fitting the energy decay curve in the first 4 ps using an exponential decay function.[134]

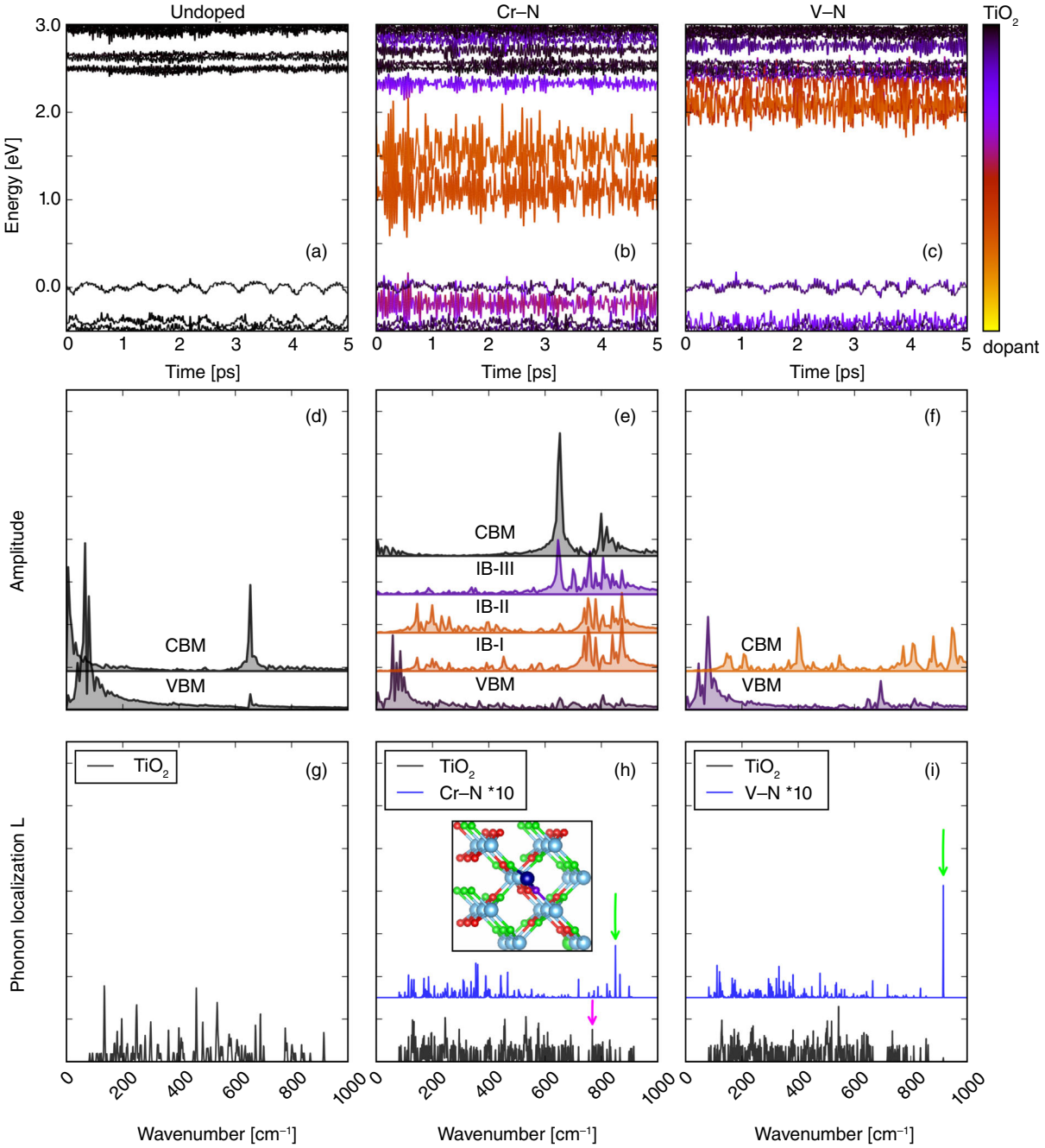

FIGURE 15 Time evolutions of the state energies near VBM and CBM for undoped, Cr—N- and V—N-codoped TiO_2 (a–c) and their FT spectra (d–f) at 300 K. The spatial localization of phonon modes (g–i). The inset in (h) shows by green color the atoms that vibrate coherently with Cr—N. In (h) and (i) the green arrows indicate the major IPMs in Cr—N- and V—N-doped TiO_2. A typical TiO_2 bulk phonon mode in Cr—N-doped TiO_2 is marked by a purple arrow. (Reprinted with permission from Reference 134. Copyright 2018 American Chemical Society)

Such a recombination timescale in nanosecond magnitude is in agreement with previous studies qualitatively.[140–145] By contrast, in Cr—N-codoped TiO_2, e–h recombination occurs within 4–5 ps with IB-I and IB-II behaving as e–h recombination centers for trapping the photogenerated electrons and holes.

Here in the dynamics of photogenerated e–h from CBM or VBM, there is no energy level crossing as shown in Figure 15b,c. Therefore, the e–h recombination is induced by the NA mechanism, and the dynamics simply depends on the NAC elements, which is shown in Figure 14g–i. The largest NAC in Cr—N-doped TiO_2 is 25 meV, which is 16 times larger than that in undoped and V—N-doped TiO_2 (around 1.5 meV). As we have discussed above, the NAC elements depend on the inverse of energy difference of the interacting states, the e–p coupling term and the nuclear velocity. In Cr—N-doped TiO_2, the energy difference between IB-I/IB-II and CBM/VBM is around 1 eV, which is approximately half of the energy difference between CBM and VBM in V—N-codoped TiO_2. This is one reason for the increasing of the NAC elements in Cr—N-codoped TiO_2. The other two factors, that is, the e–p coupling and nuclear velocity, depend on the phonon excitation and properties.

It is known that doping impurities in semiconductors will induce IPMs, which mainly couples with the impurity bands and may scatter and couple with bulk phonon modes.[146–148] These modes can be determined by calculating the phonon spatial localization (labeled as L).[146] The localization of the phonon mode s on the (group of) atom(s) α is $L_\alpha^s = \sum_{J=x,y,z}^{I\in\alpha} \left(e_{IJ}^s\right)^2$, where e_{IJ}^s is the eigenvector of the dynamical matrix corresponds to the phonon mode s. In V—N-codoped TiO_2, one can easily distinguish a major IPM at 920 cm^{-1} (Figure 15i), which has negligible coupling with TiO_2 bulk modes. It is the stretching mode between V and N atoms. However, in Cr—N-codoped TiO_2, as shown in Figure 15h, the coupling between the IPM with the TiO_2 bulk modes is much stronger. The most localized IPM at 820 cm^{-1} is marked by the green arrow in Figure 15h. As indicated by green colored atoms in the inset in Figure 15h, even for this major IPM, there are about half of the TiO_2 atoms in the supercell vibrate coherently with the Cr—N impurity. Thus the IPM in Cr—N-codoped TiO_2 can be thought to have a delocalized character. Zhang et al.[134] proposed that such delocalized character originates from the excess charge induced by Cr—N codoping.

From the analysis of e–p coupling and the frozen phonon investigations Zhang et al. proposed that the delocalized IPMs in Cr—N-doped TiO_2 induces the fast e–h recombination. First, the e–p coupling of the IBs in Cr—N-doped TiO_2 is stronger than the V 3*d* contributed CBM and N/O 2*p* contributed VBM in V—N-codoped TiO_2, which can be seen from the energy fluctuation amplitude as shown in Figure 15b,c. Second, because of the delocalized character of IPM in Cr—N-codoped TiO_2, besides the impurity contributed IBs, the CBM and VBM of Cr—N-codoped TiO_2 are coupled with IPMs as well, which can be seen from the FT spectra in Figure 15e. Zhang et al. proposed that such a coherent e–p coupling between the interacting states increase the NAC elements. In contrast, in V—N-doped TiO_2, only the V 3*d* contributed CBM has strong coupling with the localized IPM (Figure 15f).

Finally, the crucial role of the delocalized IPMs in the e–h recombination in Cr—N-codoped TiO_2 was confirmed by the frozen phonon NAMD investigations, in which the specific modes can be selected and the excited carrier dynamics coupled with these modes can be studied.[134] As shown in Figure 16a,b, when the IPMs or Cr—N-codoped TiO_2 are excited, the energies of the impurity induced bands (IB-I and IB-II) oscillate severely because of the strong e–p coupling. Along with such strong oscillation, the e–h recombination occurs at around 5 ps. By contrast, if a typical bulk phonon mode in Cr—N-codoped TiO_2 (marked by the pink arrow in Figure 15h) is excited, the e–h recombination is significantly suppressed as shown in Figure 16c,d and the timescale can be as long as nanosecond. In V—N-codoped TiO_2, one can see from Figure 16e,f, even when the major IPM is excited, the e–h recombination is still very slow because this IPM is a localized IPM and it only couples with the V 3*d* contributed CBM.

Zhang et al.[134] proposed that the important role of the delocalized IPMs can be applied to different kinds of doping systems. They investigated other mono- and codoping TiO_2 systems to confirm this point. To quantitatively understand the correlation between the IPM localization and the e–h recombination timescale, a localization factor was defined as $F_{LOC} = L_{impurity}/L_{total}$ to be a measure of the localization level of IPMs. Here L_{total} and $L_{impurity}$ are the total spatial localization of the IPM and the projection onto the doping atoms, whereby a larger F_{LOC} suggests a more localized IPM. It is shown in Figure 17 that there is an exponential dependence between F_{LOC} and the e–h recombination time at 300 K, convincing that F_{LOC} is a key parameter determining the e–h recombination timescale. There are several factors that can affect the F_{LOC}. First, it depends on the compensation of the dopants significantly. Figure 17 shows that all the noncompensate codoping and monodoping systems have small F_{LOC}, that is, delocalized IPMs. This is because the excess charge in the noncompensated doping systems induces coupling with TiO_2 atoms around the dopants and makes the IPMs to be delocalized. Second, the dopant mass is another important factor. If we compare Mo—C and V—N doping systems, which are both compensated doping, Mo—C has a lower F_{LOC}. This is because Mo is a much heavier element than C, therefore, the Mo—C stretching IPM is split into two modes. The higher one at 1,100 cm^{-1}, which is mostly associated with C atom, is strongly localized. Yet the lower IPM at 100 cm^{-1}, associated with Mo atom, has strong coupling with the TiO_2 acoustic bulk phonons, making this IPM to be delocalized. Therefore, the e–h recombination in Mo—C is faster than that in V—N and Nb—N. Zhang et al.[134] proposed that the compensated *n–p* codoping with light dopants in wide band gap semiconductors will have long e–h recombination time, which is the ideal doping scheme.

8 | DYNAMICS OF PHOTOGENERATED SPIN HOLE CURRENT IN CU-DOPED MOS_2

The NAMD simulations can also be used to investigate the spin-polarized systems. It was proposed that fully spin-polarized hole current can be generated by photoexcitation of the impurity states in MoS_2 monolayer with S partially substituted by Cu and will relax to the ground state within its lifetime. Therefore, the lifetime of the photogenerated spin hole current determines the applications of such kind of materials in spintronics. Zhao et al.[149] used NAMD simulations to study the dynamics of spin-polarized hole in Cu-doped MoS_2 monolayer.

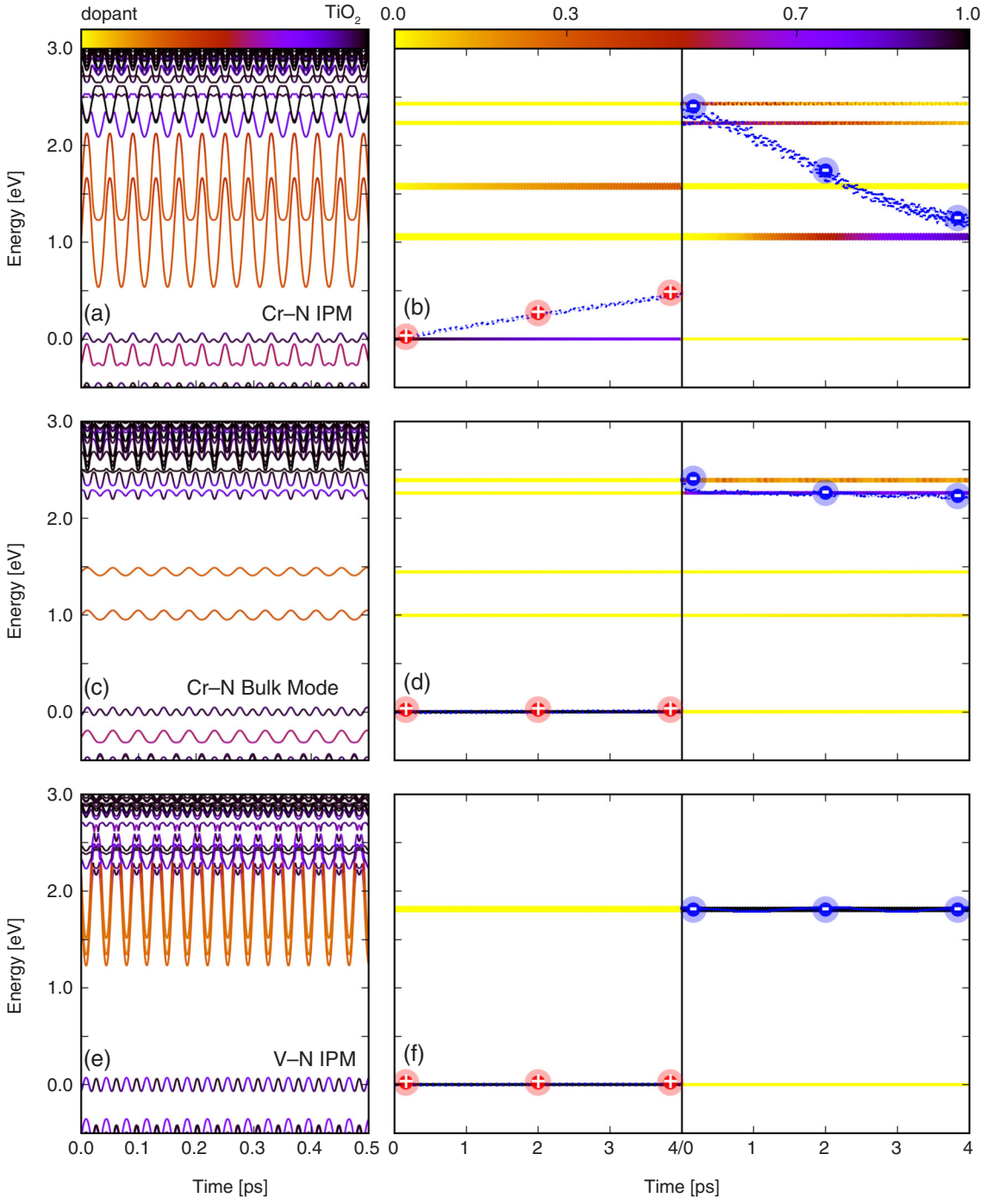

FIGURE 16 Frozen phonon NAMD results for time evolutions of the energy states near VBM and CBM and the averaged time-dependent e–h energy relaxation for Cr—N- and V—N-codoped TiO_2. (a, b) IPM for Cr—N-doped TiO_2. (c, d) One bulk mode for Cr—N-doped TiO_2. (e, f) IPM for V—N-doped TiO_2. The energy reference is the average VBM energy and the color map indicates hole localization. (Reprinted with permission from Reference 134. Copyright 2018 American Chemical Society)

Figure 18 shows the spin-polarized band structure, DOS and orbital distribution of the impurity states for the system with 8.3% Cu doping. As proposed by Zhao et al.[150] in a previous theoretical work, one single Cu doping introduces a magnetic moment of $1\mu_B$, which is contributed by the unpaired 4*d* electron of coordinated Mo atoms. A strong ferromagnetic (FM) order can be established by the super-exchange between the local spin of each atom and the Curie temperature was estimated to be around the room temperature. From the band structure shown in Figure 18a, one can see that the Cu substitution introduces four localized impurity states (labeled as State 1–4) and there is a spin-conserved band gap of 0.24 eV at the Γ point between the spin up VBM and CBM. The electrons in impurity State 1 and 2 contribute to the establishment of FM order. Fully spin-polarized hole current can be generated by photoexcitation.[151]

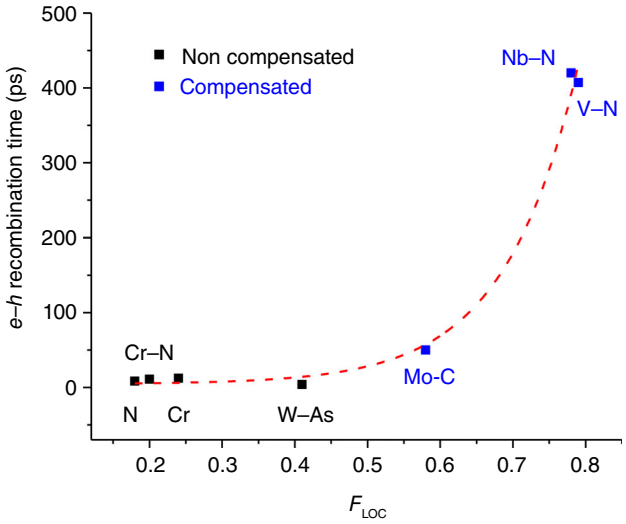

FIGURE 17 The e–h recombination time in different doped TiO_2. The fitting exponential correlation is shown in dashed lines. (Reprinted with permission from Reference 134. Copyright 2018 American Chemical Society)

As indicated by the arrow in Figure 18a, the spin-polarized hole can be generated from State 1 or 2. And once the hole relaxes across the E_f, the spin-polarized hole current disappears. Figure 19a–d shows the time-dependent energy evolutions of the four impurity states and their FT spectra in 3 ps at 100 and 50 K. The impurity states have larger energy fluctuation

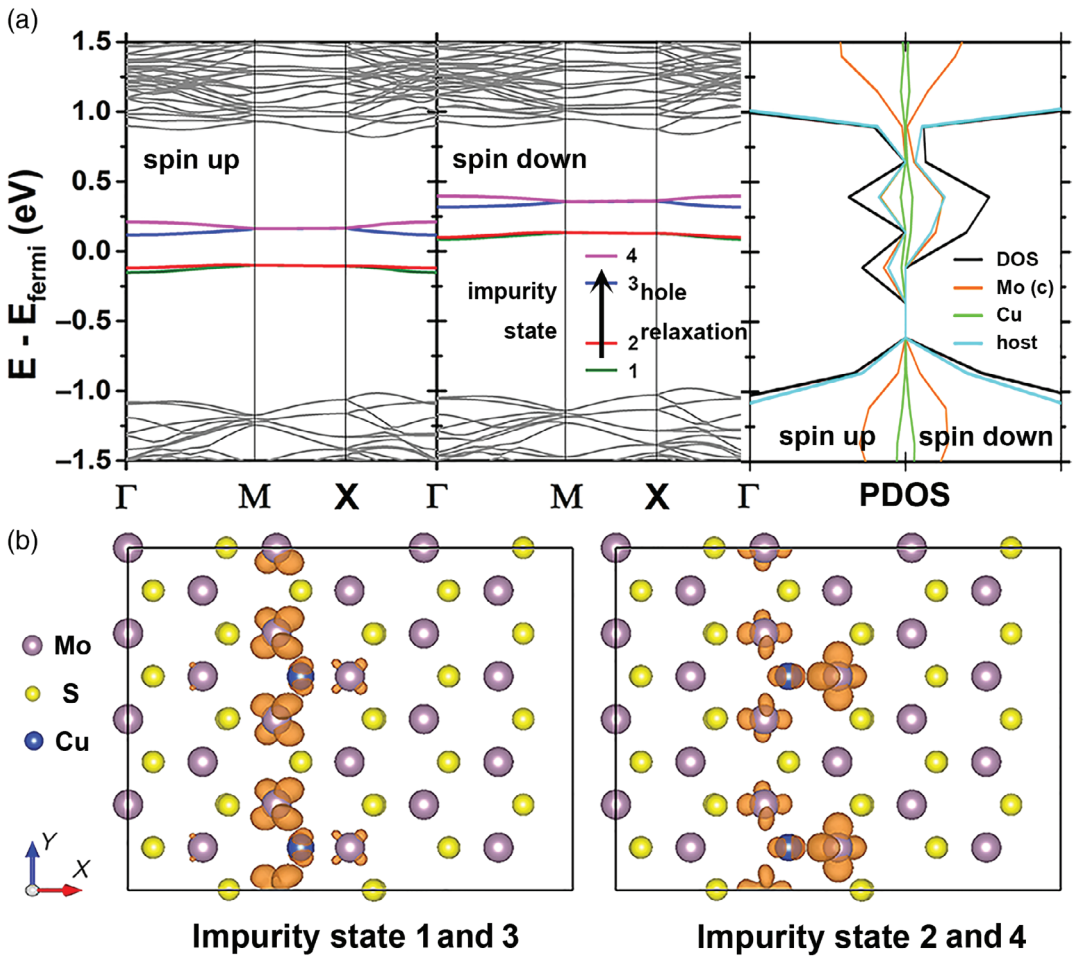

FIGURE 18 The spin-polarized band structure and the projected density of states (PDOS) (a) and the orbital spatial distribution of the Cu-doped MoS_2 (b). The total density of states (DOS) is projected on the coordinated Mo atoms, the Cu impurity atoms and the rest of the MoS_2 host in the supercell. The isosurface value in (b) is set at $0.002e/Bohr^3$. The process of spin hole relaxation within the impurity states is indicated by the arrow in panel a. (Reprinted with permission from Reference 149. Copyright 2017 American Physical Society)

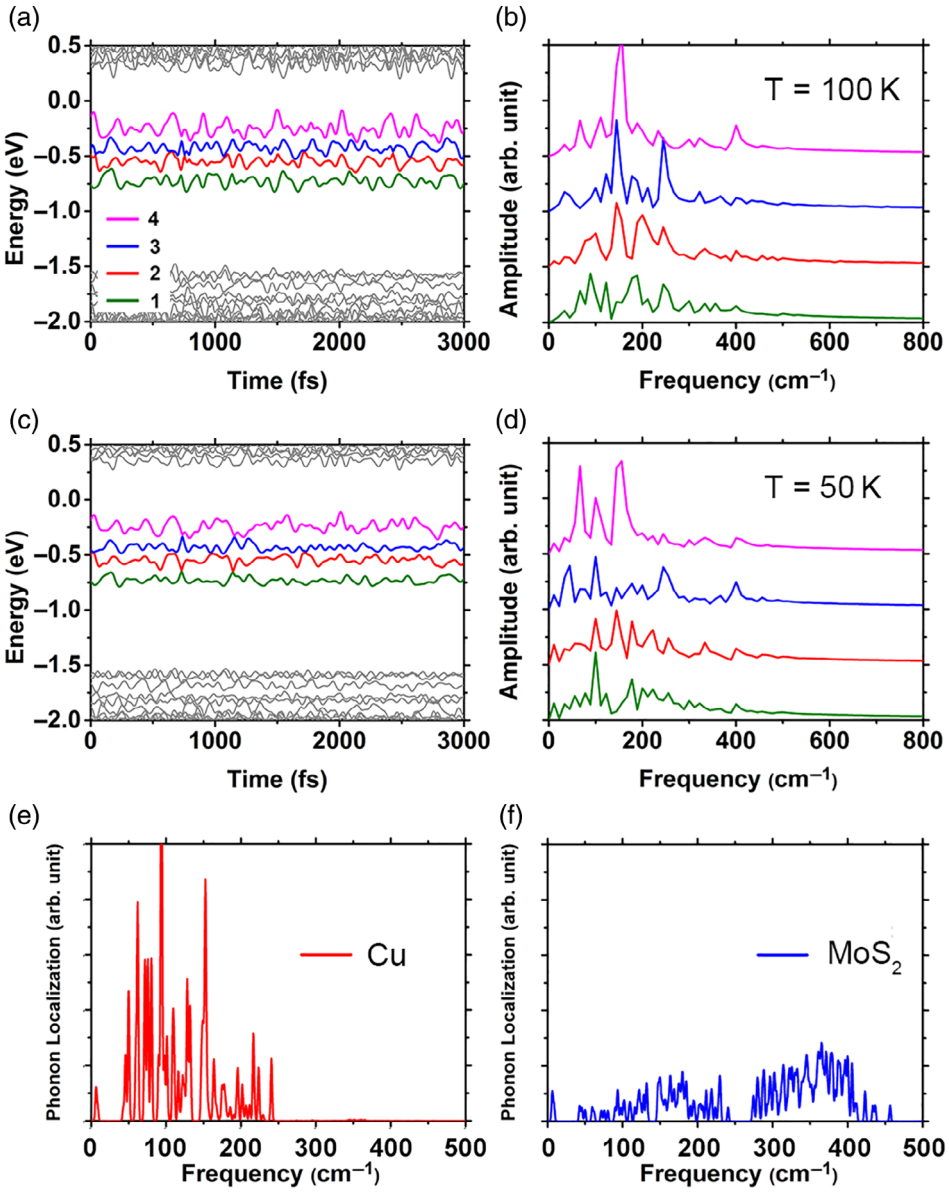

FIGURE 19 Time-dependent evolution of the energy of the impurity states at Γ point (a, c) and the FT spectra to the autocorrelation function of the energy evolution (b, d) at 100 and 50 K, respectively. The color legend is the same as in Figure 18a. The spatial localization of each normal phonon mode projected on the Cu impurity and MoS_2 host (e, f), respectively. (Reprinted with permission from Reference 149. Copyright 2017 American Physical Society)

amplitudes than the bulk states due to the stronger e–p coupling. From the FT spectra the dominate phonon modes contribute to e–p coupling can be obtained as shown in Figure 19b,d. It can be seen that the impurity states mainly coupled to the acoustic phonons below 240 cm^{-1}.[152] This point was further confirmed by calculating the phonon localization projected on Cu impurity shown in Figure 19e. Comparing Figure 19e,f one can find that the Cu IPMs couple with bulk modes in MoS_2 strongly. The scattering between the impurity and the bulk phonon modes within a range induces the violent energy fluctuation of the impurity states.

Similar to the AD and NA spatial charge transfer process, Zhao et al.[149] defined AD and NA processes for the energy relaxation. In the NAMD simulation, the averaged energy of excited electron or hole can be written as:

$$\bar{\varepsilon} = \sum_k \rho_k \varepsilon_k \tag{9}$$

Here, ρ_k is the population of the adiabatic state k, namely $c_k^* c_k$. Taking the time-derivative of Equation (9) one can get

$$\frac{d\bar{\varepsilon}}{dt} = \sum_k \left(\frac{d\rho_k}{dt} \varepsilon_k + \rho_k \frac{d\varepsilon_k}{dt} \right) \tag{10}$$

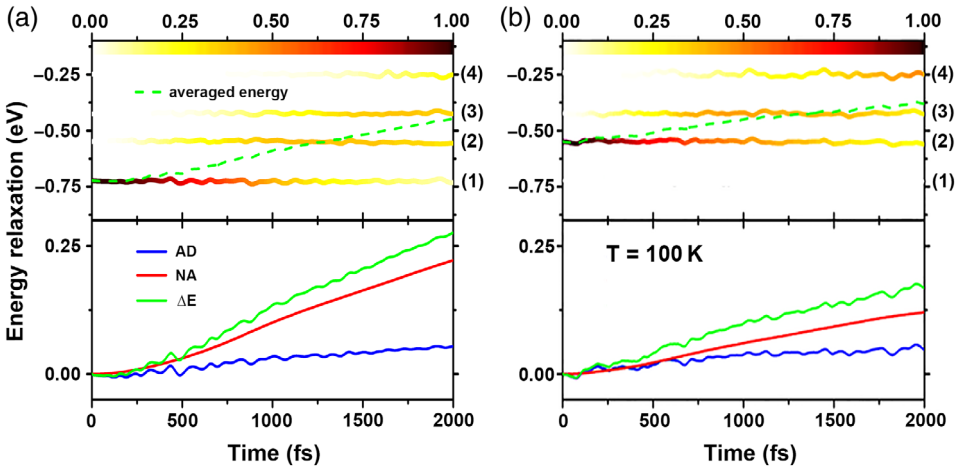

FIGURE 20 The dynamics of a photogenerated hole at 100 K. The averaged energy of the hole and the population on each impurity state (in the upper panel), the AD and NA contributions to the energy relaxation (in the lower panel) with the initial state specified at the impurity State 1 (a) and 2 (b), respectively. (Reprinted with permission from Reference 149. Copyright 2017 American Physical Society)

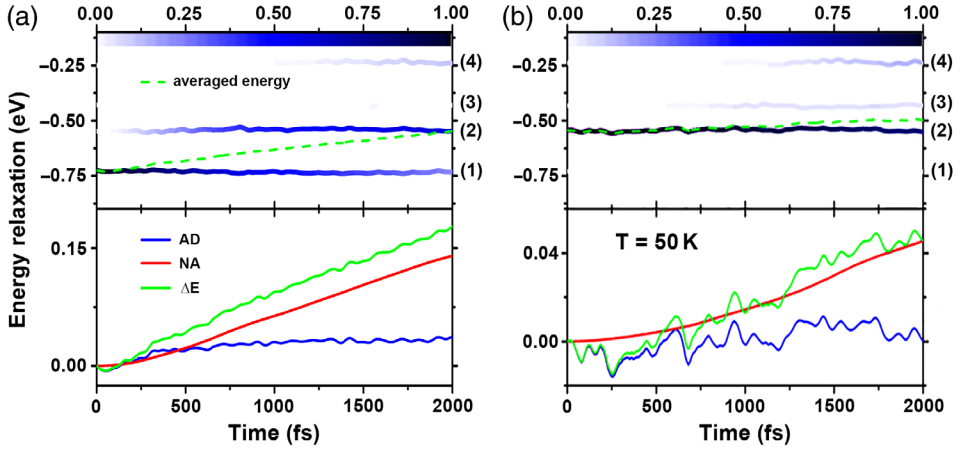

FIGURE 21 The dynamics of a photogenerated hole at 50 K. The averaged energy of the hole and the population on each impurity state (in the upper panel), the AD and NA contributions to the energy relaxation (in the lower panel) with the initial state specified at the impurity State 1 (a) and 2 (b), respectively. (Reprinted with permission from Reference 149. Copyright 2017 American Physical Society)

For the first term, the change of the averaged energy is determined by the change of the occupation of each adiabatic state, and it was defined as the NA term. The second term is due to the energy change of each adiabatic state while the population on it is fixed, and it was defined as the AD contribution to the energy relaxation.

Figures 20 and 21 show the energy relaxation along with the NA and AD contributions of photogenerated spin hole current at 100 and 50 K. At both temperatures, the hole relaxation happens by a band-by-band process. The energy relaxation shows approximately a linear correlation with the time. The NA process of energy relaxation follows the adiabatic process which is in the scale of hundreds of femtoseconds. However, the lifetime of the photogenerated spin hole current depends on the temperature significantly. When the temperature is decreased from 100 to 50 K, the hole relaxation across the bands is strongly suppressed. This is because the decreasing of the phonon occupation will induce a phonon bottleneck. Zhao et al.[149] proposed that the initial hole generation and the phonon excitation are the two key factors for the lifetime of the photogenerated spin-polarized hole.

Although in this work only the photogenerated spin-polarized hole lifetime is investigated, it shows the potential of NAMD application on the spin dynamics simulation. In NAMD simulations, the scattering of the phonons with the spin-polarized carriers are naturally included. Therefore, it is possible to study the inelastic spin transport problems, which is mainly determined by the charge–phonon interaction. If the spin–orbit coupling (SOC) is further included, the spin flip dynamics are possible to be investigated.

9 | SUMMARY AND PERSPECTIVES

This review has summarized our recent theoretical studies of excited carrier dynamics in different condensed matter systems using ab initio time-dependent NAMD simulations based on surface hopping and TDDFT implemented in the Hefei-NAMD

code.[56] The charge transfer dynamics at different interfaces, nonradiative e–h recombination process in semiconductors, and the spin-polarized hole dynamics were discussed. In these different dynamical processes, the excited carrier dynamics are found to be strongly affected by the phonon excitation and e–p coupling. At molecule/solid interface, as we have discussed in CH_3OH/TiO_2, H_2O/LAO/STO, and C_{60}/MoS_2 the charge transfer from the molecular orbitals to the electronic bands of the solid substrate are usually dominated by the AD charge transfer, which is provoked by phonon excitation. This is due to the high DOS of the solid around the molecular orbitals. At TMD interfaces, the phonon provoked AD charge transfer can induce ultrafast interlayer charge transfer or phonon-coupled charge oscillation. The timescale of AD charge transfer process is determined by the period of the coupled phonons. The nonradiative e–h recombination in TiO_2 and the spin-polarized hole dynamics in doped MoS_2 are dominated simply by the NA mechanism, which is determined by the NAC term. As we have discussed, the NAC term also strongly depends on the e–p coupling and phonon excitation. The properties of defect phonons play a crucial role in the e–h recombination at defect sites.

Besides the works discussed in this review, we propose that ab initio NAMD simulations can be extended into broader research area based on further development method. Currently, we are developing several different new aspects in Hefei-NAMD including:

1. *The nuclear quantum effects.* Based on CPA approximation, the ab initio MD, which are used to obtain the nuclear trajectory, can be replaced by ring polymer MD based on path integral technique.[153] In this case, the influence of the nuclear quantum effects on the excited carrier dynamics can be studied. We propose that such effects are important for systems containing light elements. For example, in CH_3OH/TiO_2 system or H_2O/TiO_2, we expect the nuclear quantum effects may induce the proton tunneling between the molecule and the TiO_2 surface, which can affect the charge transfer dynamics significantly.
2. *The spin–orbit coupling.* We have used Hefei-NAMD to study the spin-polarized hole dynamics in Cu-doped MoS_2. Yet for broader applications in spintronics, the SOC effects needs to be considered. There are two representation for the SOC included NAMD: the spin diabatic and spin adiabatic representations.[154] In the spin diabatic representation, the spin-polarized KS orbitals are used as basis sets and the SOC contribute to the off-diagonal elements in the Hamiltonian, which determines the probability of spin flip. In the spin adiabatic representation, the spinor orbitals are used as basis sets. With the SOC NAMD, it is possible to investigate the spin dynamics including the spin flip processes. We propose that it has important applications in spintronics.
3. *The exciton effects.* As we have discussed, the exciton effects are important in 2D systems. The exciton wave functions can be obtained from GW + BSE method. By using the exciton wave functions as basis sets, it is possible to get the exciton dynamics, which can be used to investigate the exciton generation, transfer and annihilation. In our implementation, we use the static screened coulomb potential matrix, namely the W in GW approximation, for the MD simulation to reduce computational expense. Under such an approximation, the dielectric environment does not change during the MD simulation.
4. *The improvement of CPA approximation.* In CPA approximation, the nuclear dynamics remains unaffected by the excited carrier. Using Δ-SCF or TDDFT method, the effects of excited carrier on the nuclear motions is possible to be included. Zhang and Lu[155] proposed a subspace formulation of the LR-TDDFT, which can be applied in large-scale calculations to obtain the forces on atoms at the excited states. Based on such a method, it is possible to combine the LR-TDDFT with NAMD simulations to improve the CPA approximation.

It should be noted that several other groups are also working in this emerging research frontier. For example, Akimov and coworkers[156] have included SOC in PYXAID code. They have also implemented Δ-SCF basis sets in small molecular system.[157] Meng and Kaxiras[45] have included the photoexcitation in the first principle simulations in TDAP. Kaxiras and Kolesov have also developed a similar code TDAP-2.0.[44] We expect that emerging research area will attract more and more interests from scientists in physics and chemistry in the future. The NAMD simulations for the excited carrier dynamics in condensed matter systems will have important applications in different research fields.

ACKNOWLEDGMENTS

J.Z. acknowledges the support of National Key Foundation of China, Department of Science and Technology, grant nos. 2017YFA0204904 and 2016YFA0200604; National Natural Science Foundation of China (NSFC), grant nos. 21421063 and 11620101003; the Fundamental Research Funds for the Central Universities of China (WK3510000005). Q.Z. acknowledges the support of NSFC, grant no. 11704363. Calculations were performed in part at the Environmental Molecular Sciences

Laboratory at the PNNL, a user facility sponsored by the DOE Office of Biological and Environmental Research and the Supercomputing Center at USTC.

CONFLICT OF INTEREST

The authors have declared no conflicts of interest for this article.

REFERENCES

1. Bernardi M, Palummo M, Grossman JC. Extraordinary sunlight absorption and one nanometer thick photovoltaics using two-dimensional monolayer materials. *Nano Lett*. 2013;*13*(8):3664–3670.
2. Fujishima A, Honda K. Electrochemical photolysis of water at a semiconductor electrode. *Nature*. 1972;*238*(5358):37–38.
3. Hong X, Kim J, Shi SF, et al. Ultrafast charge transfer in atomically thin MoS_2/WS_2 heterostructures. *Nat Nanotechnol*. 2014;*9*(9):682–686.
4. O'Regan B, Grätzel M. A low-cost, high-efficiency solar cell based on dye-sensitized colloidal TiO_2 films. *Nature*. 1991;*353*(6346):737–740.
5. Ummartyotin S, Infahsaeng Y. A comprehensive review on ZnS: From synthesis to an approach on solar cell. *Renew Sustain Energy Rev*. 2016;*55*:17–24.
6. Singh R, Singh PK, Singh V, Bhattacharya B, Johari R, Khan ZH. New class of lead free perovskite material for low-cost solar cell application. *Mater Res Bull*. 2018;*97*:572–577.
7. Docherty CJ, Parkinson P, Joyce HJ, et al. Ultrafast transient terahertz conductivity of monolayer MoS_2 and WSe_2 grown by chemical vapor deposition. *ACS Nano*. 2014;*8*(11):11147–11153.
8. Korn T, Heydrich S, Hirmer M, Schmutzler J, Schller C. Low-temperature photocarrier dynamics in monolayer MoS_2. *Appl Phys Lett*. 2011;*99*(10):102109.
9. Kumar N, Cui Q, Ceballos F, He D, Wang Y, Zhao H. Exciton–exciton annihilation in $MoSe_2$ monolayers. *Phys Rev B*. 2014;*89*(12):125427.
10. Shi H, Yan R, Bertolazzi S, et al. Exciton dynamics in suspended monolayer and few-layer MoS_2 2D crystals. *ACS Nano*. 2013;*7*(2):1072–1080.
11. Nie Z, Long R, Sun L, et al. Ultrafast carrier thermalization and cooling dynamics in few-layer MoS_2. *ACS Nano*. 2014;*8*(10):10931–10940.
12. Wang H, Zhang C, Chan W, Tiwari S, Rana F. Ultrafast response of monolayer molybdenum disulfide photodetectors. *Nat Commun*. 2015;*6*(1):8831.
13. Ceballos F, Bellus MZ, Chiu HY, Zhao H. Ultrafast charge separation and indirect exciton formation in a MoS_2–$MoSe_2$ van der Waals heterostructure. *ACS Nano*. 2014;*8*(12):12717–12724.
14. Aryasetiawan F, Gunnarsson O. The GW method. *Rep Prog Phys*. 1998;*61*(3):237–312.
15. Onida G, Reining L, Rubio A. Electronic excitations: Density-functional versus many-body Green's-function approaches. *Rev Mod Phys*. 2002;*74*:601–659.
16. Rohlfing M, Wang NP, Krüger P, Pollmann J. Image states and excitons at insulator surfaces with negative electron affinity. *Phys Rev Lett*. 2003;*91*(256):802.
17. Thygesen KS, Rubio A. Renormalization of molecular quasiparticle levels at metal–molecule interfaces: Trends across binding regimes. *Phys Rev Lett*. 2009;*102*:046802.
18. Van Schilfgaarde M, Kotani T, Faleev S. Quasiparticle self-consistent *GW* theory. *Phys Rev Lett*. 2006;*96*(22):226402.
19. Albrecht S, Onida G, Reining L. *Ab initio* calculation of the quasiparticle spectrum and excitonic effects in Li_2O. *Phys Rev B*. 1997;*55*(16):10278–10281.
20. Albrecht S, Reining L, Del Sole R, Onida G. *Ab initio* calculation of excitonic effects in the optical spectra of semiconductors. *Phys Rev Lett*. 1998;*80*(20):4510–4513.
21. Benedict LX, Shirley EL, Bohn RB. Optical absorption of insulators and the electron–hole interaction: An *ab initio* calculation. *Phys Rev Lett*. 1998;*80*(20):4514–4517.
22. Ferreira F, Ribeiro RM. Improvements in the GW and Bethe–Salpeter-equation calculations on phosphorene. *Phys Rev B*. 2017;*96*:115431.
23. Jiang H. Revisiting the *GW* approach to *d*- and *f*-electron oxides. *Phys Rev B*. 2018;*97*:245132.
24. Onida G, Reining L, Godby RW, Del Sole R, Andreoni W. *Ab initio* calculations of the quasiparticle and absorption spectra of clusters: The sodium tetramer. *Phys Rev Lett*. 1995;*75*(5):818–821.
25. Rohlfing M, Louie SG. Electron–hole excitations in semiconductors and insulators. *Phys Rev Lett*. 1998;*81*(11):2312–2315.
26. Appel H, Gross EKU, Burke K. Excitations in time-dependent density-functional theory. *Phys Rev Lett*. 2002;*90*(4):043005.
27. Petersilka M, Gossmann UJ, Gross EKU. Excitation energies from time-dependent density-functional theory. *Phys Rev Lett*. 1996;*76*(8):1212–1215.
28. Pavanello M, Auerbach DJ, Wodtke AM, Blanco-Rey M, Alducin M, Kroes GJ. Adiabatic energy loss in hyperthermal H atom collisions with Cu and Au: A basis for testing the importance of nonadiabatic energy loss. *J Phys Chem Lett*. 2013;*4*(21):3735–3740.
29. Shuai Q, Kaufmann S, Auerbach DJ, Schwarzer D, Wodtke AM. Evidence for electron–hole pair excitation in the associative desorption of H_2 and D_2 from Au(111). *J Phys Chem Lett*. 2017;*8*(7):1657–1663.
30. Wodtke AM. Electronically non-adiabatic influences in surface chemistry and dynamics. *Chem Soc Rev*. 2016;*45*(13):3641–3657.
31. Dou W, Subotnik JE. Perspective: How to understand electronic friction. *J Chem Phys*. 2018;*148*(23):230901.
32. Head-Gordon M, Tully JC. Molecular dynamics with electronic frictions. *J Chem Phys*. 1995;*103*(23):10137–10145.
33. Markland TE, Ceriotti M. Nuclear quantum effects enter the mainstream. *Nat Rev Chem*. 2018;*2*(3):0109.
34. Nijamudheen A, Akimov AV. Quantum dynamics effects in photocatalysis. In: Gosh S, editor. *Visible light-active photocatalysis*. Weinheim, Germany: Wiley-VCH Verlag GmbH & Co. KGaA, 2018; p. 527–566.
35. Savchenko I, Gu B, Heine T, Jakowski J, Garashchuk S. Nuclear quantum effects on adsorption of H_2 and isotopologues on metal ions. *Chem Phys Lett*. 2017;*670*:64–70.
36. Tully JC. Perspective: Nonadiabatic dynamics theory. *J Chem Phys*. 2012;*137*(22):22A301.
37. Curchod BFE, Rothlisberger U, Tavernelli I. Trajectory-based nonadiabatic dynamics with time-dependent density functional theory. *Chemphyschem*. 2013;*14*(7):1314–1340.
38. Tully JC. Mixed quantum-classical dynamics. *Faraday Discuss*. 1998;*110*:407–419.
39. Wang L, Akimov A, Prezhdo OV. Recent progress in surface hopping: 2011–2015. *J Phys Chem Lett*. 2016;*7*(11):2100–2112.
40. Barbatti M. Nonadiabatic dynamics with trajectory surface hopping method. *WIREs Comput Mol Sci*. 2011;*1*(4):620–633.
41. Tully JC. Molecular dynamics with electronic transitions. *J Chem Phys*. 1990;*93*(2):1061–1071.
42. Fiedler SL, Eloranta J. Nonadiabatic dynamics by mean-field and surface-hopping approaches: Energy conservation considerations. *Mol Phys*. 2010;*108*(11):1471–1479.
43. Andrade X, Strubbe D, De Giovannini U, et al. Real-space grids and the Octopus code as tools for the development of new simulation approaches for electronic systems. *Phys Chem Chem Phys*. 2015;*17*(47):31371–31396.
44. Kolesov G, Grånäs O, Hoyt R, Vinichenko D, Kaxiras E. Real-time TD-DFT with classical ion dynamics: Methodology and applications. *J Chem Theory Comput*. 2016;*12*(2):466–476.

45. Meng S, Kaxiras E. Real-time, local basis-set implementation of time-dependent density functional theory for excited state dynamics simulations. *J Chem Phys*. 2008;*129*(5):054110.
46. Akimov AV. Libra: An open-source "methodology discovery" library for quantum and classical dynamics simulations. *J Comput Chem*. 2016;*37*(17):1626–1649.
47. Akimov AV, Prezhdo OV. The PYXAID program for non-adiabatic molecular dynamics in condensed matter systems. *J Chem Theory Comput*. 2013;*9*(11):4959–4972.
48. Akimov AV, Prezhdo OV. Advanced capabilities of the PYXAID program: Integration schemes, decoherence effects, multiexcitonic states, and field-matter interaction. *J Chem Theory Comput*. 2014;*10*(2):789–804.
49. Barbatti M, Granucci G, Persico M, et al. The on-the-fly surface-hopping program system Newton-X: Application to *ab initio* simulation of the nonadiabatic photodynamics of benchmark systems. *J Photochem Photobiol A Chem*. 2007;*190*(2–3):228–240.
50. Du L, Lan Z. An on-the-fly surface-hopping program JADE for nonadiabatic molecular dynamics of polyatomic systems: Implementation and applications. *J Chem Theory Comput*. 2015;*11*(4):1360–1374.
51. Sato K, Pradhan E, Asahi R, Akimov AV. Charge transfer dynamics at the boron subphthalocyanine chloride/$C_6$0 interface: Non-adiabatic dynamics study with Libra-X. *Phys Chem Chem Phys*. 2018;*20*(39):25275–25294.
52. Tapavicza E, Tavernelli I, Rothlisberger U. Trajectory surface hopping within linear response time-dependent density-functional theory. *Phys Rev Lett*. 2007;*98*(2):023001.
53. Craig CF, Duncan WR, Prezhdo OV. Trajectory surface hopping in the time-dependent Kohn–Sham approach for electron-nuclear dynamics. *Phys Rev Lett*. 2005;*95*(16):163001.
54. Fischer SA, Habenicht BF, Madrid AB, Duncan WR, Prezhdo OV. Regarding the validity of the time-dependent Kohn–Sham approach for electron-nuclear dynamics via trajectory surface hopping. *J Chem Phys*. 2011;*134*(2):024102.
55. Long R, Prezhdo OV, Fang W. Nonadiabatic charge dynamics in novel solar cell materials. *WIREs Comput Mol Sci*. 2017;*7*(3):e1305.
56. Zheng, Q., Zhao, C., & Chu, W.. Hefei-NAMD. Available from: http://staff.ustc.edu.cn/∼zhaojin/code.html
57. Kresse G, Hafner J. *Ab initio* molecular dynamics for liquid metals. *Phys Rev B*. 1993a;*47*(1):558–561.
58. Kresse G, Hafner J. *Ab initio* molecular dynamics for open-shell transition metals. *Phys Rev B*. 1993b;*48*(17):13115–13118.
59. Kresse G, Hafner J. *Ab initio* molecular-dynamics simulation of the liquid-metalamorphous-semiconductor transition in germanium. *Phys Rev B*. 1994;*49*(20):14251–14269.
60. Runge E, Gross EK. Density-functional theory for time-dependent systems. *Phys Rev Lett*. 1984;*52*(12):997–1000.
61. Billeter SR, Curioni A. Calculation of nonadiabatic couplings in density-functional theory. *J Chem Phys*. 2005;*122*(3):034105.
62. Hammes-Schiffer S, Tully JC. Proton transfer in solution: Molecular dynamics with quantum transitions. *J Chem Phys*. 1994;*101*(6):4657–4667.
63. Jaeger HM, Fischer S, Prezhdo OV. Decoherence-induced surface hopping. *J Chem Phys*. 2012;*137*(22):22A545.
64. Zheng Q, Saidi WA, Xie Y, et al. Phonon-assisted ultrafast charge transfer at van der Waals heterostructure interface. *Nano Lett*. 2017;*17*(10):6435–6442.
65. Popescu V, Zunger A. Extracting E versus $\vec{k}$ effective band structure from supercell calculations on alloys and impurities. *Phys Rev B*. 2012;*85*:085201.
66. Zheng, Q. VASPBandUnfolding. Available from: https://github.com/QijingZheng/VaspBandUnfolding.
67. Chen X, Burda C. The electronic origin of the visible-light absorption properties of C-, N- and S-doped TiO_2 nanomaterials. *J Am Chem Soc*. 2008;*130*(15):5018–5019.
68. Feng X, Zhu K, Frank AJ, Grimes CA, Mallouk TE. Rapid charge transport in dye-sensitized solar cells made from vertically aligned single-crystal rutile TiO_2 nanowires. *Angew Chem Int Ed*. 2012;*51*(11):2727–2730.
69. Han X, Kuang Q, Jin M, Xie Z, Zheng L. Synthesis of titania nanosheets with a high percentage of exposed (001) facets and related photocatalytic properties. *J Am Chem Soc*. 2009;*131*(9):3152–3153.
70. Ingram DB, Linic S. Water splitting on composite plasmonic-metal/semiconductor photoelectrodes: Evidence for selective plasmon-induced formation of charge carriers near the semiconductor surface. *J Am Chem Soc*. 2011;*133*(14):5202–5205.
71. Li H, Bian Z, Zhu J, et al. Mesoporous titania spheres with tunable chamber stucture and enhanced photocatalytic activity. *J Am Chem Soc*. 2007;*129*(27):8406–8407.
72. Liu S, Yu J, Jaroniec M. Tunable photocatalytic selectivity of hollow TiO_2 microspheres composed of anatase polyhedra with exposed {001} facets. *J Am Chem Soc*. 2010;*132*(34):11914–11916.
73. Livraghi S, Paganini MC, Giamello E, Selloni A, Di Valentin C, Pacchioni G. Origin of photoactivity of nitrogen-doped titanium dioxide under visible light. *J Am Chem Soc*. 2006;*128*(49):15666–15671.
74. Naldoni A, Allieta M, Santangelo S, et al. Effect of nature and location of defects on bandgap narrowing in black TiO_2 nanoparticles. *J Am Chem Soc*. 2012;*134*(18):7600–7603.
75. Santra PK, Kamat PV. Mn-doped quantum dot sensitized solar cells: A strategy to boost efficiency over 5%. *J Am Chem Soc*. 2012;*134*(5):2508–2511.
76. Swierk JR, Mallouk TE. Design and development of photoanodes for water-splitting dye-sensitized photoelectrochemical cells. *Chem Soc Rev*. 2013;*42*(6):2357–2387.
77. Wang J, Tafen DN, Lewis JP, et al. Origin of photocatalytic activity of nitrogen-doped TiO_2 nanobelts. *J Am Chem Soc*. 2009;*131*(34):12290–12297.
78. Xiang Q, Yu J, Jaroniec M. Synergetic effect of MoS_2 and graphene as cocatalysts for enhanced photocatalytic H_2 production activity of TiO_2 nanoparticles. *J Am Chem Soc*. 2012;*134*(15):6575–6578.
79. Yang HG, Liu G, Qiao SZ, et al. Solvothermal synthesis and photoreactivity of anatase TiO_2 nanosheets with dominant {001} facets. *J Am Chem Soc*. 2009;*131*(11):4078–4083.
80. Youngblood JW, Lee SHA, Kobayashi Y, et al. Photoassisted overall water splitting in a visible light-absorbing dye-sensitized photoelectrochemical cell. *J Am Chem Soc*. 2009;*131*(3):926–927.
81. Yu J, Low J, Xiao W, Zhou P, Jaroniec M. Enhanced photocatalytic CO_2-reduction activity of anatase TiO_2 by coexposed {001} and {101} facets. *J Am Chem Soc*. 2014;*136*(25):8839–8842.
82. Chu W, Saidi WA, Zheng Q, et al. Ultrafast dynamics of photongenerated holes at a CH_3OH/TiO_2 rutile interface. *J Am Chem Soc*. 2016;*138*(41):13740–13749.
83. Fischer SA, Duncan WR, Prezhdo OV. *Ab initio* nonadiabatic molecular dynamics of wet-electrons on the TiO_2 surface. *J Am Chem Soc*. 2009;*131*(42):15483–15491.
84. Chen Z, Zhang Q, Luo Y. Experimental identification of ultrafast reverse hole transfer at the interface of the photoexcited methanol/graphitic carbon nitride system. *Angew Chem Int Ed*. 2018;*57*(19):5320–5324.
85. Kolesov G, Vinichenko D, Tritsaris GA, Friend CM, Kaxiras E. Anatomy of the photochemical reaction: Excited-state dynamics reveals the C–H acidity mechanism of methoxy photo-oxidation on titania. *J Phys Chem Lett*. 2015;*6*(9):1624–1627.
86. Onda K, Li B, Zhao J, Jordan KD, Yang J, Petek H. Wet electrons at the H_2O/TiO_2(110) surface. *Science*. 2005;*308*(5725):1154–1158.
87. Zhao J, Li B, Onda K, Feng M, Petek H. Solvated electrons on metal oxide surfaces. *Chem Rev*. 2006;*106*(10):4402–4427.

88. Koitaya T, Nakamura H, Yamashita K. First-principle calculations of solvated electrons at protic solvent–TiO_2 interfaces with oxygen vacancies. *J Phys Chem C*. 2009;*113*(17):7236–7245.
89. Petek H, Zhao J. Ultrafast interfacial proton-coupled electron transfer. *Chem Rev*. 2010;*110*(12):7082–7099.
90. Zhao J, Li B, Jordan KD, Yang J, Petek H. Interplay between hydrogen bonding and electron solvation on hydrated TiO_2(110). *Phys Rev B*. 2006;*73*(19):195309.
91. Li B. Ultrafast interfacial proton-coupled electron transfer. *Science*. 2006;*311*(5766):1436–1440.
92. Migani A, Mowbray DJ, Iacomino A, Zhao J, Petek H, Rubio A. Level alignment of a prototypical photocatalytic system: Methanol on TiO_2(110). *J Am Chem Soc*. 2013;*135*(31):11429–11432.
93. Migani A, Mowbray DJ, Zhao J, Petek H, Rubio A. Quasiparticle level alignment for photocatalytic interfaces. *J Chem Theory Comput*. 2014;*10*(5):2103–2113.
94. Zhao J, Yang J, Petek H. Theoretical study of the molecular and electronic structure of methanol on a TiO_2(110) surface. *Phys Rev B*. 2009;*80*(23):235416.
95. Wang Y, Guo H, Zheng Q, Saidi WA, Zhao J. Tuning solvated electrons by polar-nonpolar oxide heterostructure. *J Phys Chem Lett*. 2018;*9*(11):3049–3056.
96. Nozik AJ. Quantum dot solar cells. *Physica E*. 2002;*14*(1–2):115–120.
97. Ross RT, Nozik AJ. Efficiency of hot-carrier solar energy converters. *J Appl Phys*. 1982;*53*(5):3813–3818.
98. Tisdale W, Williams K, Timp B, Norris D, Aydil E, Zhu XY. Hot electron transfer from semiconductor nanocrystals. *Science*. 2010;*328*(5985):1543–1548.
99. Williams F, Nozik AJ. Solid-state perspectives of the photoelectrochemistry of semiconductor electrolyte junctions. *Nature*. 1984;*312*(5989):21–27.
100. Abuabara SG, Rego LG, Batista VS. Influence of thermal fluctuations on interfacial electron transfer in functionalized TiO_2 semiconductors. *J Am Chem Soc*. 2005;*127*(51):18234–18242.
101. Akimov AV, Neukirch AJ, Prezhdo OV. Theoretical insights into photoinduced charge transfer and catalysis at oxide interfaces. *Chem Rev*. 2013;*113*(6):4496–4565.
102. Kilina SV, Craig CF, Kilin DS, et al. *Ab initio* time-domain study of phonon-assisted relaxation of charge carriers in a PbSe quantum dot *ab initio* time-domain study of phonon-assisted relaxation of charge carriers in a PbSe quantum dot. *J Phys Chem C*. 2007;*111*(12):4871–4878.
103. Kilina SV, Kilin DS, Prezhdo OV. Breaking the phonon bottleneck in PbSe and CdSe quantum dots: Time-domain density functional theory of charge carrier relaxation. *ACS Nano*. 2009;*3*(1):93–99.
104. Kilina SV, Kilin DS, Prezhdo VV, Prezhdo OV. Theoretical study of electron–phonon relaxation in PbSe and CdSe quantum dots: Evidence for phonon memory. *J Phys Chem C*. 2011;*115*(44):21641–21651.
105. Kim JW, Park H, Zhu X. Charge transport and separation dynamics at the C_{60}/GaAs(001) interface. *J Phys Chem C*. 2014;*118*(6):2987–2991.
106. Li L, Long R, Prezhdo OV. Charge separation and recombination in two-dimensional MoS_2/WS_2: Time-domain *ab initio* modeling. *Chem Mater*. 2017;*29*(6):2466–2473.
107. Long R, Fang WH, Prezhdo OV. Strong interaction at the perovskite/TiO_2 interface facilitates ultrafast photoinduced charge separation: A nonadiabatic molecular dynamics study. *J Phys Chem C*. 2017;*121*(7):3797–3806.
108. Park H, Gutierrez M, Wu X, Kim W, Zhu XY. Optical probe of charge separation at organic/inorganic semiconductor interfaces. *J Phys Chem C*. 2013;*117*(21):10974–10979.
109. Rego LGC, Batista VS. Quantum dynamics simulations of interfacial electron transfer in sensitized TiO_2 semiconductors. *J Am Chem Soc*. 2003;*125*(26):7989–7997.
110. Zhong Y, Trinh MT, Chen R, et al. Molecular helices as electron acceptors in high-performance bulk heterojunction solar cells. *Nat Commun*. 2015;*6*:8242.
111. Guo H, Zhao C, Zheng Q, et al. Superatom molecular orbital as an interfacial charge separation state. *J Phys Chem Lett*. 2018;*9*(12):3485–3490.
112. Feng M, Zhao J, Petek H. Atomlike, hollow-core-bound molecular orbitals of C_{60}. *Science*. 2008;*320*(5874):359–362.
113. Appavoo K, Nie W, Blancon JC, Even J, Mohite AD, Sfeir MY. Ultrafast optical snapshots of hybrid perovskites reveal the origin of multiband electronic transitions. *Phys Rev B*. 2017;*96*:195308.
114. Frost JM, Whalley LD, Walsh A. Slow cooling of hot polarons in halide perovskite solar cells. *ACS Energy Lett*. 2017;*2*(12):2647–2652.
115. Fu J, Xu Q, Han G, et al. Hot carrier cooling mechanisms in halide perovskites. *Nat Commun*. 2017;*8*(1):1300.
116. Nozik AJ. Spectroscopy and hot electron relaxation dynamics in semiconductor quantum wells and quantum dots. *Annu Rev Phys Chem*. 2001;*52*(1):193–231.
117. Nozik AJ, Beard MC, Luther JM, Law M, Ellingson RJ, Johnson JC. Semiconductor quantum dots and quantum dot arrays and applications of multiple exciton generation to third-generation photovoltaic solar cells. *Chem Rev*. 2010;*110*(11):6873–6890.
118. Benisty H. Reduced electron–phonon relaxation rates in quantum-box systems: Theoretical analysis. *Phys Rev B*. 1995;*51*:13281–13293.
119. Benisty H, Sotomayor-Torrès CM, Weisbuch C. Intrinsic mechanism for the poor luminescence properties of quantum-box systems. *Phys Rev B*. 1991;*44*:10945–10948.
120. Bockelmann U, Bastard G. Phonon scattering and energy relaxation in two-, one-, and zero-dimensional electron gases. *Phys Rev B*. 1990;*42*:8947–8951.
121. Bockelmann U, Egeler T. Electron relaxation in quantum dots by means of Auger processes. *Phys Rev B*. 1992;*46*:15574–15577.
122. Lee C, Yan H, Brus L, Heinz T, Hone J, Ryu S. Anomalous lattice vibrations of single- and few-layer MoS_2. *ACS Nano*. 2010;*4*(5):2695–2700.
123. Li Y, Wang H, Xie L, Liang Y, Hong G, Dai H. MoS_2 nanoparticles grown on graphene: An advanced catalyst for the hydrogen evolution reaction. *J Am Chem Soc*. 2011;*133*(19):7296–7299.
124. Splendiani A, Sun L, Zhang Y, et al. Emerging photoluminescence in monolayer MoS_2. *Nano Lett*. 2010;*10*(4):1271–1275.
125. Ji Z, Hong H, Zhang J, et al. Robust stacking-independent ultrafast charge transfer in MoS_2/WS_2 bilayers. *ACS Nano*. 2017;*11*(12):12020–12026.
126. Lee CH, Lee GH, Van Der Zande AM, et al. Atomically thin p–n junctions with van der Waals heterointerfaces. *Nat Nanotechnol*. 2014;*9*(9):676–681.
127. Zhu X, Monahan NR, Gong Z, Zhu H, Williams KW, Nelson CA. Charge transfer excitons at van der Waals interfaces. *J Am Chem Soc*. 2015;*137*(26):8313–8320.
128. Zheng Q, Xie Y, Lan Z, Prezhdo OV, Saidi WA, Zhao J. Phonon-coupled ultrafast interlayer charge oscillation at van der Waals heterostructure interfaces. *Phys Rev B*. 2018;*97*(20):205417.
129. Gong Y, Lin J, Wang X, et al. Vertical and in-plane heterostructures from WS_2/MoS_2 monolayers. *Nat Mater*. 2014;*13*(12):1135–1142.
130. Miller B, Steinhoff A, Pano B, et al. Long-lived direct and indirect interlayer excitons in van der Waals heterostructures. *Nano Lett*. 2017;*17*(9):5229–5237.
131. Liang L, Meunier V. First-principles Raman spectra of MoS_2, WS_2 and their heterostructures. *Nanoscale*. 2014;*6*:5394–5401.
132. Zhang J, Wang J, Chen P, et al. Observation of strong interlayer coupling in MoS_2/WS_2 heterostructures. *Adv Mater*. 2016;*28*(10):1950–1956.
133. Wang H, Bang J, Sun Y, et al. The role of collective motion in the ultrafast charge transfer in van der Waals heterostructures. *Nat Commun*. 2016;*7*:11504.
134. Zhang L, Zheng Q, Xie Y, et al. Delocalized impurity phonon induced electron–hole recombination in doped semiconductors. *Nano Lett*. 2018;*18*(3):1592–1599.
135. Asahi R, Morikawa T, Ohwaki T, Aoki K, Taga Y. Visible-light photocatalysis in nitrogen-doped titanium oxides. *Science*. 2001;*293*(5528):269–271.
136. Batzill M, Morales EH, Diebold U. Influence of nitrogen doping on the defect formation and surface properties of TiO_2 rutile and anatase. *Phys Rev Lett*. 2006;*96*:026103.
137. Feng N, Wang Q, Zheng A, et al. Understanding the high photocatalytic activity of (B, Ag)-Codoped TiO_2 under solar-light irradiation with XPS, solid-state NMR, and DFT calculations. *J Am Chem Soc*. 2013;*135*(4):1607–1616.
138. Gai Y, Li J, Li SS, Xia JB, Wei SH. Design of narrow-gap TiO_2: A passivated codoping approach for enhanced photoelectrochemical activity. *Phys Rev Lett*. 2009;*102*(3):036402.

139. Zhu W, Qiu X, Iancu V, et al. Band gap narrowing of titanium oxide semiconductors by noncompensated anion-Cation codoping for enhanced visible-Light photoactivity. *Phys Rev Lett*. 2009;*103*(22):226401.
140. Bahnemann DW, Hilgendorff M, Memming R. Charge carrier dynamics at TiO_2 particles: Reactivity of free and trapped holes. *J Phys Chem B*. 1997;*101*(21): 4265–4275.
141. Fujihara K, Izumi S, Ohno T, Matsumura M. Time-resolved photoluminescence of particulate TiO_2 photocatalysts suspended in aqueous solutions. *J Photochem Photobiol A Chem*. 2000;*132*(1–2):99–104.
142. Furube A, Asahi T, Masuhara H, Yamashita H, Anpo M. Charge carrier dynamics of standard TiO_2 catalysts revealed by femtosecond diffuse reflectance spectroscopy. *J Phys Chem B*. 1999;*103*(16):3120–3127.
143. Ozawa K, Emori M, Yamamoto S, et al. Electron–hole recombination time at TiO_2 single-crystal surfaces: Influence of surface band bending. *J Phys Chem Lett*. 2014;*5*(11):1953–1957.
144. Xu M, Gao Y, Moreno EM, et al. Photocatalytic activity of bulk TiO_2 anatase and rutile single crystals using infrared absorption spectroscopy. *Phys Rev Lett*. 2011;*106*(13):138302.
145. Yamada Y, Kanemitsu Y. Determination of electron and hole lifetimes of rutile and anatase TiO_2 single crystals. *Appl Phys Lett*. 2012;*101*(13):133907.
146. Estreicher SK, Gibbons TM, Kang B, Bebek MB. Phonons and defects in semiconductors and nanostructures: Phonon trapping, phonon scattering and heat flow at heterojunctions. *J Appl Phys*. 2014, jan;*115*(1):012012.
147. Holland MG. Phonon scattering in semiconductors from thermal conductivity studies. *Phys Rev*. 1964;*134*(2A):A471–A480.
148. Shakouri A. Recent developments in semiconductor thermoelectric physics and materials. *Ann Rev Mater Res*. 2011;*41*(1):399–431.
149. Zhao C, Zheng Q, Wu J, Zhao J. *Ab initio* nonadiabatic molecular dynamics investigation on the dynamics of photogenerated spin hole current in Cu-doped MoS_2. *Phys Rev B*. 2017;*96*(13):134308.
150. Zhao C, Jin C, Wu J, Ji W. Magnetism in molybdenum disulphide monolayer with sulfur substituted by 3*d* transition metals. *J Appl Phys*. 2016;*120*(14):144305.
151. Wang XL. Proposal for a new class of materials: Spin gapless semiconductors. *Phys Rev Lett*. 2008;*100*(15):156404.
152. Molina-Sánchez A, Wirtz L. Phonons in single-layer and few-layer MoS_2 and WS_2. *Phys Rev B*. 2011;*84*(15):155413.
153. Shushkov P, Li R, Tully JC. Ring polymer molecular dynamics with surface hopping. *J Chem Phys*. 2012;*137*(22):22A549.
154. Mai S, Marquetand P, González L. A general method to describe intersystem crossing dynamics in trajectory surface hopping. *Int J Quant Chem*. 2015;*115*(18): 1215–1231.
155. Zhang X, Lu G. Subspace formulation of time-dependent density functional theory for large-scale calculations. *J Chem Phys*. 2015;*143*(6):064110.
156. Li W, Zhou L, Prezhdo OV, Akimov AV. Spin–orbit interactions greatly accelerate nonradiative dynamics in lead halide perovskites. *ACS Energy Lett*. 2018;*3*(9): 2159–2166.
157. Pradhan E, Sato K, Akimov AV. Non-adiabatic molecular dynamics with ΔSCF excited states. *J Phys Condens Matter*. 2018;*30*(48):484002.

How to cite this article: Zheng Q, Chu W, Zhao C, et al. Ab initio nonadiabatic molecular dynamics investigations on the excited carriers in condensed matter systems. *WIREs Comput Mol Sci*. 2019;9:e1411. https://doi.org/10.1002/wcms.1411